A&A manuscript no.
(will be inserted by hand later)

Your thesaurus codes are:
06(08.19.4; 08.14.1; 02.07.1; 02.08.1; 02.03.3; 02.09.1)

ASTRONOMY AND ASTROPHYSICS
17.4.1996

Gravitational radiation from convective instabilities in Type II supernova explosions

Ewald Müller and H.-Thomas Janka

Max-Planck-Institut für Astrophysik, Karl-Schwarzschild-Str. 1, D-85740 Garching, Germany

Received ; accepted

Abstract. We present two- and three-dimensional simulations of convective instabilities during the first second of a Type II supernova explosion. Convective overturn occurs in two distinct, spatially well separated regions: (i) inside the proto-neutron star immediately below the neutrinosphere ($r \lesssim 50$ km) and (ii) in the neutrino-heated "hot-bubble" region interior to the outward propagating revived shock wave (100 km $\lesssim r \lesssim$ 1000 km). We have calculated the gravitational wave signature of both convective instabilities including the quadrupole waveforms, the energy spectra, and the total amount of the emitted gravitational wave energy. Moreover, we have estimated the amplitude and energy of gravitational waves associated with the anisotropic neutrino emission that is caused by the convective transport of neutrinos and by aspherical perturbations of temperature and density in the neutrinospheric region.

For a supernova located at a distance of 10 kpc the maximum dimensionless gravitational wave amplitudes due to convective mass motions range from $|h^{\rm TT}| \approx 2 \times 10^{-22}$ for the three-dimensional simulation to $|h^{\rm TT}| \approx 7 \times 10^{-21}$ for the most strongly radiating two-dimensional model. The total emitted energy varies from $10^{-13}\ M_\odot c^2$ to $2 \times 10^{-9}\ M_\odot c^2$. The convective mass motions inside the proto-neutron star produce a stronger signal than convection in region (ii) with up to a factor of 10 larger amplitudes and 1000 times more gravitational wave energy. Because of smaller convective eddies and structures and slower overturn velocities, the wave amplitudes of three-dimensional models are more than a factor of 30 smaller, and the energy emitted in gravitational waves is more than 3 orders of magnitude less than in the corresponding two-dimensional situation.

In two dimensions the gravitational wave amplitude associated with the anisotropic emission of neutrinos can be larger (factor 2) than the wave amplitude due to mass motions in the proto-neutron star, although the energy in the neutrino tidal field is 100 times smaller. In three dimensions the neutrino gravitational wave amplitude is reduced by a factor of about 10 and the gravitational wave energy by a factor of roughly 100 relative to the two-dimensional results. Nevertheless, the neutrino tidal field is more than a factor of 10 larger than the gravitational wave amplitude from mass motions and the corresponding gravitational wave energies can be of similar size.

Most of the gravitational radiation from convection inside the proto-neutron star is emitted in the frequency band 100–1000 Hz, while convective motions in the hot-bubble region generate waves from several 100 Hz down to a few Hz. Gravitational waves from the anisotropic neutrino emission have most power at frequencies between some 10 Hz and a few 100 Hz and a low-frequency contribution at about 1 Hz to several Hz.

Features in the gravitational-wave signal from the neutrino-heated region are well correlated with structures in the neutrino signal, both being associated with sinking and rising lumps of matter and with temporal variations of aspherical accretion flows towards the proto-neutron star. A simultaneous measurement of both signals would impose important contraints on the dynamics of Type II supernovae and theoretical models of the explosion mechanism.

Key words: supernovae: general – stars: neutron – gravitation: waves – hydrodynamics – convection – instabilities

1. Introduction

Currently the most promising model of Type II supernova explosions, which are powered by the gravitational binding energy released in the collapse of the iron-nickel core of a massive star with a main sequence mass of $8\ M_\odot \lesssim M \lesssim 25\ M_\odot$, relies on the so-called delayed explosion mechanism by neutrino heating (Wilson 1985; Bethe & Wilson 1985; Wilson et al. 1986; Colgate 1989; Janka 1993). According to this mechanism energy is deposited in the layers between the nascent neutron star and the stalled prompt supernova shock during a period of a few 100 ms by absorption of a minor fraction (between 1 and 10%) of the neutrinos emitted from the collapsed core. This neutrino-energy deposition produces a radiation dominated hot-bubble region and eventually causes the supernova explosion by reviving the stalled shock wave.

Send offprint requests to: E. Müller

After the shock wave stalls ($\approx$ 10 ms after bounce) and before the delayed neutrino heating mechanism begins to become effective ($\approx$ 100 ms after bounce) the outer parts of the proto-neutron star are convectively unstable because, firstly, the deleptonization occuring in the shocked matter outside the neutrinosphere produces a negative lepton gradient and because, secondly, the weakening (and the eventual stalling) of the prompt shock wave gives rise to a negative entropy gradient in the same region. According to Epstein (1979) this is a sufficient condition for convective motion to occur. This is a situation commonly encountered in most supernova simulations (Burrows 1987; Burrows & Lattimer 1988; Bruenn 1993). The existence of these instabilities was demonstrated in several multi-dimensional hydrodynamical simulations (Burrows & Fryxell 1992, 1993; Burrows et al. 1995; Janka & Müller 1993a,b; 1995a,b; Müller 1993; Müller & Janka 1994).

Noting that the hot bubble is convectively unstable, Bethe (1990) and Colgate (1989; see also Colgate et al. 1993) pointed out that this situation may give rise to a dynamical overturn of hot, neutrino-heated, rising material and cold postshock matter, and can lead to large-scale deviations from spherically symmetrical supernova explosions. This instability was indeed found in numerical simulations (Burrows et al. 1995; Herant et al. 1992, 1994; Janka & Müller 1993b, 1995a, 1996; Yamada et al. 1993; Shimizu et al. 1993, 1994; Müller & Janka 1994; see, however, Miller et al. 1993).

Provided sufficient energy is deposited by neutrinos in the postshock matter an energetically typical Type II supernova explosion ($E_{\rm exp} \approx 10^{51}$ erg) results. Whether this explosion mechanism is successful or not depends very sensitively on the neutrino flux that is emitted from the neutrinosphere of the hot proto-neutron star and its decay with time (Janka 1993; Janka & Müller 1995a,b, 1996).

While propagating outward through the stellar envelope the shock wave will produce density and pressure stratifications, which are Rayleigh-Taylor unstable in the neighbourhood of composition interfaces, i.e. near nuclear burning shells (Bandiera 1984; Benz & Thielemann 1989). This third kind of instability (actually a set of instabilities) in Type II supernova explosions has numerically been investigated in great detail (Fryxell et al. 1991; Hachisu et al. 1990, 1991; Herant & Benz 1991, 1992; Müller et al. 1991) and will not be considered further here.

In Table 1 an overview over the different types of hydrodynamical instabilities in Type II supernova explosions is presented and some important characteristics are summarized.

The non-spherical stratification and mass flow resulting from these instabilities, or, more precisely, the time-dependent mass quadrupole moment, is a potential source of gravitational radiation (for a recent review, see Thorne 1995). Obviously, only convection inside the proto-neutron star and inside the hot-bubble region is a promising source, because both convective regions are located at relatively small radii (see Table 1). The instabilities in the stellar envelope occur at such large radii that no strong gravitational wave signal can be expected. Hence, we have only analysed the gravitational wave signature of the two former instabilities. In addition, we have attempted to estimate the gravitational wave amplitudes and energy associated with the anisotropic neutrino emission from our models (Epstein 1978, Turner 1978). In particular the convective processes around the neutrinosphere can lead to anisotropies of the neutrino luminosity which are caused by convective transport of neutrinos and by temperature and density variations in the neutrinospheric region.

In the following we present the first detailed investigation to determine the gravitational radiation from post-bounce convective motions in Type II supernova explosions. The results are based on several two-dimensional hydrodynamical simulations and on two three-dimensional ones (Janka & Müller 1995a, 1996; Müller 1993). Special attention is therefore focussed on the comparison of the characteristics of the convective overturn in the two- and three-dimensional cases and on the corresponding differences of the gravitational-wave emission. Our analysis is in some sense complementary to other investigations, in which the gravitational radiation from collapsing, rotating cores was computed (Mönchmeyer et al. 1991; Bonazzola & Marck 1993; Zwerger 1995; Müller & Zwerger 1995). In rotational core collapse the gravitational radiation results from a time-dependent quadrupole moment due to a coherent, large-scale deviation from spherical symmetry caused by the action of centrifugal forces, whereas the gravitational radiation emitted from the convectively unstable regions is produced by small-scale statistical deviations from sphericity. Another potential source of gravitational radiation from Type II supernova are asphericities which can already exist in the Si- and O-shells of the progenitor star (Bazan & Arnett 1994) and which might be amplified during core collapse (Burrows & Hayes 1996).

The paper is organized as follows. In Sect. 2 we describe the results of our two- and three-dimensional simulations with the main emphasis being put on the simulations of convection inside the proto-neutron star, because the results for the convective overturn processes in the hot-bubble region have already been presented and discussed earlier (see Janka & Müller 1995a, 1996). In Sect. 3 first the formalism is described which was used to calculate the gravitational wave signature of our models. Thereafter, the quadrupole waveforms of the gravitational radiation, the frequency-dependent spectra of the wave amplitudes, the spectral energy densities (i.e., the differential energy emitted at different frequencies), and the total, i.e. spectrally integrated, energies emitted in gravitational waves are given for all our models. Finally, we summarize our results and discuss their implications in Sect. 4.

2. Simulations of convection

All simulations were performed with a modified version of the explicit hydrodynamical code PROMETHEUS (Fryxell et al. 1989; Müller et al. 1991), which is a direct Eulerian implementation of the P*iecewise* P*arabolic* M*ethod* of Colella & Woodward (1984).

Table 1. Hydrodynamical instabilities in Type II supernova explosions

type of instability	**convection inside the proto-neutron star** (unstable mass region: $0.7\ M_\odot \lesssim m(r) \lesssim 1.20\ M_\odot$ for iron core masses $\approx 1.3 - 1.4\ M_\odot$)	**convection in the hot-bubble region** (unstable mass region: $1.25\ M_\odot \lesssim m(r) \lesssim 1.40\ M_\odot$ for iron core masses $\approx 1.3 - 1.4\ M_\odot$)	**Rayleigh-Taylor instabilities in the stellar envelope** at composition and shell interfaces after shock passage
cause of instability	prompt deleptonization burst and failure of prompt shock causing unstable entropy and/or lepton gradients	energy deposition by neutrinos causing unstable entropy gradient in layers behind stalled and revived shock wave	unsteady shock propagation through stellar envelope causing unstable density and pressure stratifications
radial location	10 (?) – 50 km	≈ 100 – 1000 km	≳ 5000 km
onset after shock formation	≈ 10 – 20 ms	≈ 50 – 80 ms	≈ 0.3 – 0.5 hrs
duration	≈ 20 ms – sec (?)	≈ 100 – 500 ms	≈ 2 – 3 hrs
convective overturn timescale	≈ 1 – 10 ms	≈ 40 – 100 ms	
maximum gravitational wave amplitude for a source at 10 kpc	$\approx 7 \times 10^{-21}$	$\approx 9 \times 10^{-22}$	
energy radiated in form of gravitational waves	$\lesssim 2 \times 10^{-9}\ M_\odot c^2$	$\lesssim 3 \times 10^{-12}\ M_\odot c^2$	
typical frequency of gravitational wave emission	100 – 1000 Hz	10 – 100 Hz	

2.1. Convection inside the proto-neutron star

The simulations concentrating on the convective processes inside the proto-neutron star have been performed neglecting effects due to neutrinos completely. This is justified, since the main purpose of the simulations was to demonstrate the existence of the convective instability inside the proto-neutron star and to reveal the relevant length scales and timescales of the convective overturn. We followed these processes only over a period of about 30–50 ms and do not expect any crucial modification of the gas flow by neutrino-energy gain or loss. In particular, the convective velocities seen in our simulations are so high that convective mixing is probably faster than neutrino diffusion.

Neutrino viscosity should also be negligible, because the Reynolds number of neutrino shear viscosity is relatively large for the considered densities $\rho \approx 10^{11}$–10^{12} g/cm^3, temperatures $T \approx$ 3–10 MeV, length scales $l \approx 10^6$ cm and velocities $u \approx 10^9$ cm/s in the convective region. Estimates based on the expressions given by van den Horn & van Weert (1981) yield for the dynamical shear viscosity of neutrinos in the diffusive regime

$$\eta_\nu \;\approx\; 3 \times 10^{23}\, \frac{T_5^2}{\rho_{12}} \quad \left[\frac{\mathrm{g}}{\mathrm{cm\ s}}\right] \tag{1}$$

and for the corresponding Reynolds number

$$\Re(\nu) \;=\; \frac{\rho u l}{\eta_\nu} \;\approx\; 3000 \left(\frac{\rho_{12}}{T_5}\right)^2 u_9\, l_6\,, \tag{2}$$

where T_5 is the temperature in 5 MeV, ρ_{12} the density in 10^{12} g/cm^3, u_9 the fluid velocity in 10^9 cm/s and l_6 the typical length scale in 10^6 cm.

All simulations were performed with an elaborate, vectorized equation of state, which contains contributions from neutrons, protons, alpha particles, and a representative heavy nucleus in nuclear statistical equilibrium. Electrons, treated as an arbitrarily degenerate and relativistic gas, positrons, and photons were taken into account.

The initial model was a spherically symmetrical (nonrotating) post-bounce model of Hillebrandt (1987) which represented the approximately 1.4 $M_\odot$ iron core of a 20 $M_\odot$ star about 12 ms after core bounce. As this model was computed with a general relativistic correction to the gravitational potential, the model had to be relaxed before it was mapped onto the multi-dimensional grid. This was achieved by evolving the model with the 1D Lagrangian hydrodynamics code of Janka (unpublished) for another 17 ms. Then all waves created by the initial force imbalance had died out.

In order to save a significant amount of computer time we used an inner boundary condition at a fixed finite radius $R_{\rm in}$ = 15 km, which corresponds to an interior mass $M_{\rm in}$ = 0.639 $M_\odot$. Hence, we did not simulate the flow in the inner part of the proto-neutron star. We assumed hydrostatic equilibrium at the inner boundary and approximated the interior mass by an equivalent central point mass. The usage of such an inner boundary is well justified for sufficiently short times, because initially the inner part of the proton-neutron star is convectively stable (see Figs. 1 and 2). Of course, one must take care that the computational grid extends far enough into the stable region.

Self-gravity of the matter in the computational domain was computed with the efficient algorithm of Müller & Steinmetz (1995), which solves Poisson's equation in integral form by an expansion into spherical harmonics. In the 3D simulations a spherically symmetrical potential was used, which results from the angular-averaged density distribution outside the inner boundary and the central point mass. As the overall matter distribution remains nearly spherically symmetrical during the evolution of the convective instability, this approximation should cause only small errors. Two-dimensional test calculations with and without a spherically symmetrical potential confirmed the smallness of the errors.

The multi-dimensional simulations were started by mapping the one-dimensional post-bounce model onto the 2D (or 3D) grid and by perturbing the radial velocity on the whole grid with a random perturbation of 10^{-3} amplitude. When reducing the perturbation to 10^{-5} the results changed only little.

2.1.1. Two-dimensional simulations

The two-dimensional simulations of convection inside the proto-neutron star were performed in spherical coordinates using a computational grid of 400 (non-equidistant) radial and 90 (equidistant) angular zones. Axial and equatorial symmetry was assumed. The radius of the inner boundary was set to 15 km (see above), while the outer edge of the grid was located at a radius of 2000 km.

In Figs. 1 and 2 the Y_e and entropy distributions, respectively, are displayed at several moments of time during the evolution. In both figures the solid curve gives the initial distribution.

The deep trough in the Y_e profile is the result of neutrino losses and deleptonization around the neutrinosphere, where neutrinos decouple from the stellar gas and where their mode of propagation changes from diffusion to free streaming. Since electron neutrinos are created when electrons and protons combine to neutrons, the gas close to the proto-neutron star "surface" quickly neutronizes and the concentration of electrons, Y_e, decreases. The entropy maxima at $M(r)$ = 0.88 $M_\odot$ and $M(r)$ = 1.26 $M_\odot$ are caused by a combination of shock propagation and post-bounce oscillations of the collapsed iron core.

Figs. 1 and 2 clearly show that for 0.87 $M_\odot \lesssim M(r) \lesssim$ 1.07 $M_\odot$ the initial entropy gradient as well as the initial Y_e gradient are negative, i.e., the stratification is convectively unstable. From the inner boundary at $M(r)$ = 0.639 $M_\odot$ out to

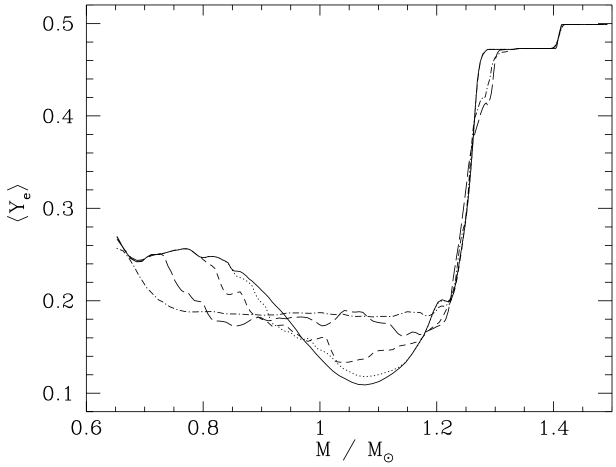

Fig. 1. Time evolution of the angular-averaged electron number fraction $\langle Y_e \rangle$ plotted versus enclosed mass $M(r)$ for a 2D simulation: solid (t = 0), dotted (t = 12 ms), short dashed (t = 14 ms), long dashed (t = 18 ms), and dash-dotted (t = 32 ms). Note that at t = 0 ms the model is spherically symmetrical

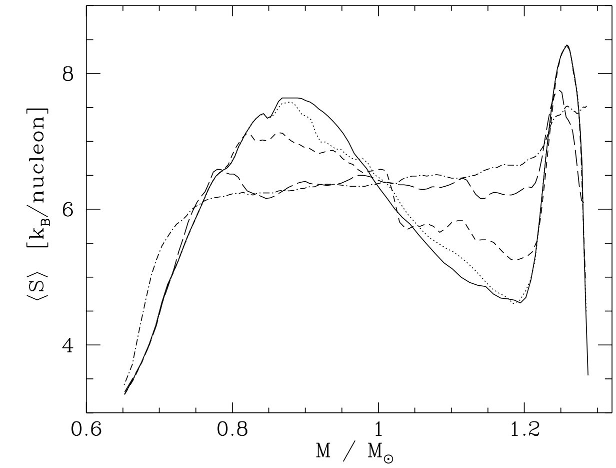

Fig. 2. Same as Fig. 1 but showing the angular-averaged (total) entropy per nucleon

$M(r)$ = 0.69 $M_\odot$ and for 0.77 $M_\odot \lesssim M(r) \lesssim$ 0.87 $M_\odot$ the Y_e gradient is negative but the entropy gradient is positive. The mass layer in between (0.69 $M_\odot \lesssim M(r) \lesssim$ 0.77 $M_\odot$) is stable as both gradients are positive. Outside the convectively unstable region the entropy gradient remains negative up to $M(r)$ = 1.2 $M_\odot$, while the initial Y_e gradient becomes positive. Even further out both gradients are positive up to the local entropy maximum at $M(r)$ = 1.26 $M_\odot$, implying a convectively stable stratification. In a narrow adjacent mass layer (1.26 $M_\odot \lesssim M(r) \lesssim$ 1.29 $M_\odot$) which is located immediately behind the shock the entropy gradient is strongly negative while the lepton gradient, which is positive at the inner edge of the layer, quickly becomes zero. According to the stability criterion this is a convectively unstable situation. We point out that such unstable stratifications can also be found in other core collapse simulations, as e.g., in post-bounce models of Bruenn (1993). Note that although the different regions may be rather narrow in terms of the mass coordinate $M(r)$, they can nevertheless have a sizable radial extension of several ten kilometers.

The evolution of the angular-averaged electron number fraction $\langle Y_e \rangle$ and of the angular-averaged entropy $\langle S \rangle$ is shown for the two-dimensional simulation in Fig. 1 and Fig. 2, respectively. While the trough in the initial $\langle Y_e \rangle$-profile is filled in, further inside the adjacent, initially stable plateau is more and more eroded due to convective undershooting. The corresponding effect can be recognized in the evolution of the angular-averaged entropy distribution, where the trough in the profile at $M(r) \approx 1.15\ M_\odot$ is filled in, while the entropy maximum at $M(r) \approx 0.9\ M_\odot$ is removed. Due to convective overshooting both profiles are also flattened out to $M(r) \approx 1.22\ M_\odot$ which is well beyond the outer edge of the convectively unstable mass layer at $M(r) = 1.07\ M_\odot$. Figs. 1 and 2 clearly exhibit convective mixing also immediately behind the shock wave in the region $1.26\ M_\odot \leq M(r) \leq 1.29\ M_\odot$ where only the entropy gradient is unstable. Here some convective over- and undershooting penetrate into the stable layers above and below and influence the $\langle Y_e \rangle$ and $\langle S \rangle$ profiles within about $0.1\ M_\odot$ around the convecting shell.

According to Figs. 1 and 2 the convective instability needs a growth time of about 10 ms before significant modifications of the entropy and lepton number distributions occur. It then takes another 10 to 20 ms to completely homogenize both the entropy and the Y_e distributions in the unstable layers and in the adjacent regions influenced by convective under- and overshooting. Note in this respect that the extent of undershooting at the inner edge of the innermost unstable region steadily increases with time and has almost reached the inner boundary of the computational grid at the end of the simulation. This may be taken as an indication that eventually the whole proto-neutron star might be involved in this process und thus neutrino transport by convective motions could be more important than diffusive transport in deleptonizing the proto-neutron star. However, only simulations which cover a longer interval of the evolution and which also consider the whole proto-neutron star can definitely confirm this possibility.

The development of the convective instability in the mantle of the proto-neutron star is further illustrated in Figs. 3 to 7. The right upper panels in Figs. 3a and 4a show that first the inner unstable layer develops Rayleigh-Taylor fingers that penetrate inward and plumes that rise outward. This is best seen from the entropy plot (Fig. 4) which shows the two entropy maxima (in orange and red) and the low-entropy zones (in blue) inside, between, and outside these maxima. The position of the shock wave is at the inner edge of the outermost blue region. The yellow-red ring immediately behind the shock marks the outer unstable layer where the convective instability requires a longer timescale (about 15–20 ms) to grow into the nonlinear regime (lower two panels in Fig. 4). The Rayleigh-Taylor fingers are subject to Kelvin-Helmholtz instabilities that lead to the formation of mushroom-like caps and strong bending of the mushroom stems. As a consequence the initially narrow fingers begin to merge into successively larger blobs (upper and lower left panels in Figs. 3a and 4a). After another 5–10 ms the whole unstable region is involved in a convective overturn (lower right panels in Figs. 3 and 4). Finally, after about 25–30 ms, the inner region is completely mixed and homogenized.

The convective mixing releases gravitational binding energy by establishing a more compact stratification in the mantle of the proto-neutron star (see also Figs. 7 and 17). The liberated binding energy is used to temporarily push the shock out to about 400 km which is more than twice its initial radius. This is illustrated in Fig. 5 which shows the evolution of the entropy distribution between 20 and 32 ms after the beginning of the simulation. The outward propagation of the shock is clearly seen, as well as the mushrooms rising up from the outer convectively unstable layer. The shock expansion comes to a halt at $t \approx$ 30–40 ms and subsequently a re-contraction sets in.

As the convective velocities reach and even partially exceed the local sound speed ($v_{\rm conv} \approx 10^9$ cm/s) strong pressure waves and even weak shock waves are generated by the convective flow. This is illustrated in Fig. 6, where the divergence of the velocity field is shown for the same four snapshots of time as displayed in Fig. 5. Besides the propagation of the shock wave, one recognizes several strong, interacting sound waves "emitted" from the convective region and propagating outward behind the supernova shock front. The convective layer itself shows a turbulent wave activity which reflects the non-stationary character of the convective overturn. Moreover, we see from Fig. 6 that the shock wave is not perfectly spherically symmetrical and exhibits large-scale deformations caused by the interaction with rising convective elements. The overall, moderately prolate deformation of the shock front along the symmetry axis of the two-dimensional computational grid for $t \gtrsim 25$ ms is produced by a large convective element that rises rapidly near the symmetry axis (see Figs. 3, 4 and 5). We point out, however, that its outward velocity may in fact be overestimated because of the imposed axial symmetry which implies that convective elements near the symmetry axis are blob-like while those at the equator are torus-like.

The convective activity inside the proto-neutron star causes significant inhomogeneities in the temperature and density stratifications as illustrated by Fig. 7. The inhomogeneities vary in time and space implying non-radial mass motions and a time-dependent mass quadrupole moment associated with the outer layers of the proto-neutron star. Both effects generate gravitational radiation with typical frequencies in the range of several hundred Hz to about one kHz (see Sect. 3). In the transition from the upper panels (at $t = 12$ ms after the start of the simulation) to the lower panels (at $t = 21$ ms) in Fig. 7 the more compact stratification of the later state is clearly visible.

Although not included in the present simulation, we may speculate about another, possibly very important effect of convection, which has implications for the explosion mechanism. Convective mixing around and below the neutrinospheric region near the proto-neutron star surface may be accompanied by an increase of the neutrino luminosities during the early

Fig. 3. Convection inside the nascent neutron star. The four panels show the time evolution of the electron number fraction Y_e in a region between 15 km and 155 km. The panels are arranged in counter-clockwise order, starting from the right upper side, and show snapshots at 12 ms, 14 ms, 18 ms, and 21 ms after the start of the 2D simulation. The colours correspond to Y_e in the range $[0.1, 0.5]$ with increasing values from blue, over green, yellow, and orange to red. Blue regions have $Y_e \lesssim 0.12$, yellow regions correspond to $0.13 \lesssim Y_e \lesssim 0.16$, orange regions to $0.16 \lesssim Y_e \lesssim 0.21$, and red ones to $Y_e \gtrsim 0.21$

Fig. 4. Same as Fig. 3 but showing the time evolution of the entropy distribution. The colour levels correspond to entropies in the range $[3.2, 12.3]$ with increasing values from blue, over dark green and yellow to red. Blue regions have $S \lesssim 5$, dark green regions correspond to $5 \lesssim S \lesssim 6$, yellow regions to $6 \lesssim S \lesssim 8$, and red regions to $8 \lesssim S \lesssim 12$

Fig. 5. Convective overturn in the proto-neutron star and transient shock expansion. The four panels show the time evolution of the entropy in a region between 15 km and 403 km. The panels are arranged in counter-clockwise order, starting from the right upper side, and show snapshots at 20 ms, 25 ms, 28 ms, and 32 ms after the start of the 2D simulation. The colour coding is the same as in Fig. 4

Fig. 6. Same as Fig. 5 but showing the evolution of the divergence of the flow field. The colour coding is chosen such that compression waves are strongly enhanced. Dependent on their strength shocks are encoded from dark blue to light blue while sound waves appear in yellow

Fig. 7. Structural effects of convective instabilities on the proto-neutron star. The four panels show two snapshots of the time evolution of the temperature distribution (left two panels) and of the logarithm of the density distribution (right two panels) in a region between 15 km and 95 km. The upper two snapshots are taken 12 ms and the two lower ones 21 ms after the start of the 2D simulation. The colours correspond to temperature values in the range 2.5×10^{10} K $\leq T \leq 1.8 \times 10^{11}$ K and to density values in the range $10.5 \leq \log \rho \leq 13.3$, both increasing from blue, over green and yellow to red. Yellow regions have a temperature of about 10^{11} K and a density of approximately 5×10^{11} g/cm^3. Below and near the neutrinospheric region which is at a density of about 10^{11} g/cm^3, density contrasts of about a factor of 2 develop and temperature differences of up to $\sim 30\%$ occur

phase of the supernova explosion. Since the convection is dynamical and violent and the gas velocities are close to the local speed of sound, neutrinos could be transported out of the dense interior of the newly-formed neutron star much faster than by diffusion. The corresponding increase of the neutrino emission may provide an important aid to the neutrino-powered explosion mechanism. Moreover, the neutron star shrinks faster due to the enhanced cooling of its surface layers. Since, in addition, the supernova shock is driven further out as a consequence of the convective settling of the outer parts of the proto-neutron star, ideal conditions for efficient neutrino-heating in the postshock region are established.

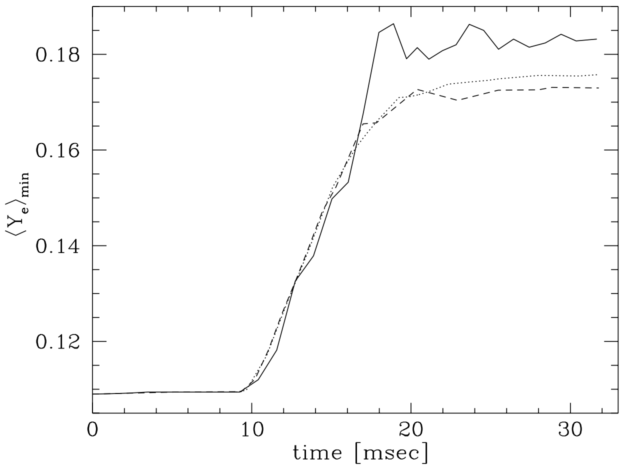

Fig. 8. Time evolution of the minimum value of the angular-averaged electron number fraction $\langle Y_e \rangle_{\rm min}$ in the convective region of the proto-neutron star: solid (2D simulation); dotted (3D simulation in a 60° sector); dashed (3D simulation in a 20° sector)

2.1.2. Three-dimensional simulations

The two three-dimensional calculations were done on a grid (r, θ, ϕ) of $320 \times 60 \times 60$ and $320 \times 20 \times 20$ zones, respectively. The non-equidistant radial zones covered the region 15 km $\leq r \leq$ 1000 km, while the equidistant angular zones covered a cone of opening angle 60° and 20°, respectively. In both simulations the cone was centered at $\theta = 90°$ and $\phi = 0°$ and periodic boundary conditions were imposed in the angular directions.

The development of the convective instability inside the proto-neutron star looks qualitatively quite similar when comparing the results of 2D and 3D simulations. The growth rates of the convective instability are practically identical, as can be seen from the time evolution of the minimum value of the angular-averaged electron number fraction $\langle Y_e \rangle_{\rm min}$ in the convective region (Fig. 8). In comparison with the 2D simulations the amount of overshooting and undershooting is somewhat smaller in the two 3D simulations which explains the smaller final $\langle Y_e \rangle_{\rm min}$, $\langle Y_e \rangle^{\rm 3D}_{\rm min} \approx 0.175$ compared to $\langle Y_e \rangle^{\rm 2D}_{\rm min} = 0.182$, by less mixing of high-Y_e matter from the layers above and below into the convective region (see also Fig. 16).

The qualitative similarity of the 2D and 3D results is also confirmed by Figs. 9 and 10, which show snapshots of the distributions of electron number fraction (Fig. 9) and of the entropy (Fig. 10) in a meridional cut of the computational domain 14 ms after the start of the simulation. The features present in Figs. 9 and 10 are qualitatively very similar to those found in the 2D simulations at the same epoch (see upper left panel of Fig. 3 and Fig. 4, respectively). However, the finger-like or blob-like structures seen in the 2D runs are actually toroidal structures (because of the assumed axial symmetry), whereas the inhomogeneities in the 3D simulations are genuine three-dimensional structures with no geometrical restrictions imposed. Their development from small fingers or bubbles to mushroom-like features which subsequently merge is illustrated in Fig. 11, which shows three snapshots of the surface $Y_e = 0.16$ at times $t = 12.2$ ms, 13.6 ms, and 16.6 ms, respectively.

In order to compare the 2D and 3D results in a more quantitative way we have performed a normal mode analysis by Fourier transforming the electron number fraction (which is a good tracer of the inhomogeneities) at different epochs of the evolution. The relative power of the turbulent motions at different wave numbers and at different radial positions inside the convectively unstable layer is shown for the 3D simulation with 60° cone in Fig. 12 by contour plots at three moments of time. A corresponding contour plot for the 2D simulation is given in Fig. 13 at $t = 13.9$ ms which is very close to the time of the second snapshot in Fig. 12. In Figs. 12 and 13 the left ordinate gives the wave number of the normal mode normalized to one quadrant $k_4 \equiv k/4 = (\pi/2)/\lambda$, while the right ordinate gives the corresponding wavelength (in degrees) of the mode. This means that the typical angular size of rising or falling lumps of matter is half this wavelength. Note that in the 3D case, we have averaged the Y_e distribution in ϕ-direction before performing the Fourier transformation. If we instead average over the distribution in θ-direction the power spectrum does not change significantly.

Figure 12 shows that the evolution of the power spectrum is characterized by small-scale features growing into large-scale ones in the whole unstable layer, an effect which reflects the successive merging of smaller Rayleigh-Taylor fingers into larger ones as well as the increasing homogenization of the convective layer by the mixing process. At $t = 16.6$ ms (third panel in Fig. 12) all power has become concentrated into structures which have a wavelength larger than about 10 degrees, while early on in the evolution (first panel of Fig. 12) a significant amount of power is contained in features with a wavelength of several degrees only. Comparing the second panel of Fig. 12 with Fig. 13 one recognizes that at the epoch of maximum convective activity the structures in the 3D simulation are only about half as large with respect to their angular extent than those in the 2D simulation. In particular, in the three-dimensional case the dominant modes have (angular) wavelengths of about 20°–30° (i.e., clump sizes of about 10°–15°), while the corre-

Fig. 9. Convection inside the nascent neutron star. The snapshot shows a meridional cut ($\phi = 0^\circ$) of Y_e 14 ms after the start of the 3D simulation with a cone of opening angle 60°. Note that the shapshot is taken at the same time as the upper left panel in Fig. 3. The radial size of the displayed region and the colour coding is the same as in Fig. 3

Fig. 10. Same as Fig. 9 but showing the evolution of the entropy distribution. The colour coding is the same as in Fig. 4

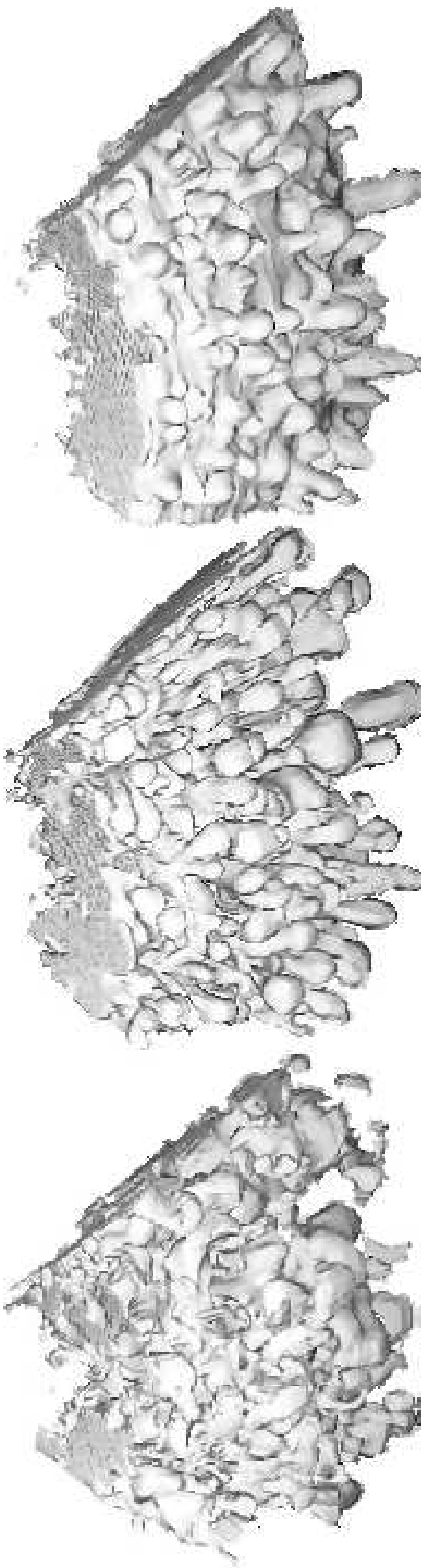

Fig. 11. Surface of constant electron fraction $Y_e = 0.160$ at $t = 12.2$ ms, 13.6 ms, and 16.6 ms (from top to bottom) for the 3D simulation that was performed in a wedge of opening angle 60° (between $\theta = 60°$ and $\theta = 120°$)

sponding values are around 40°–60° (i.e., clump sizes of approximately 20°–30°) in the two-dimensional simulation.

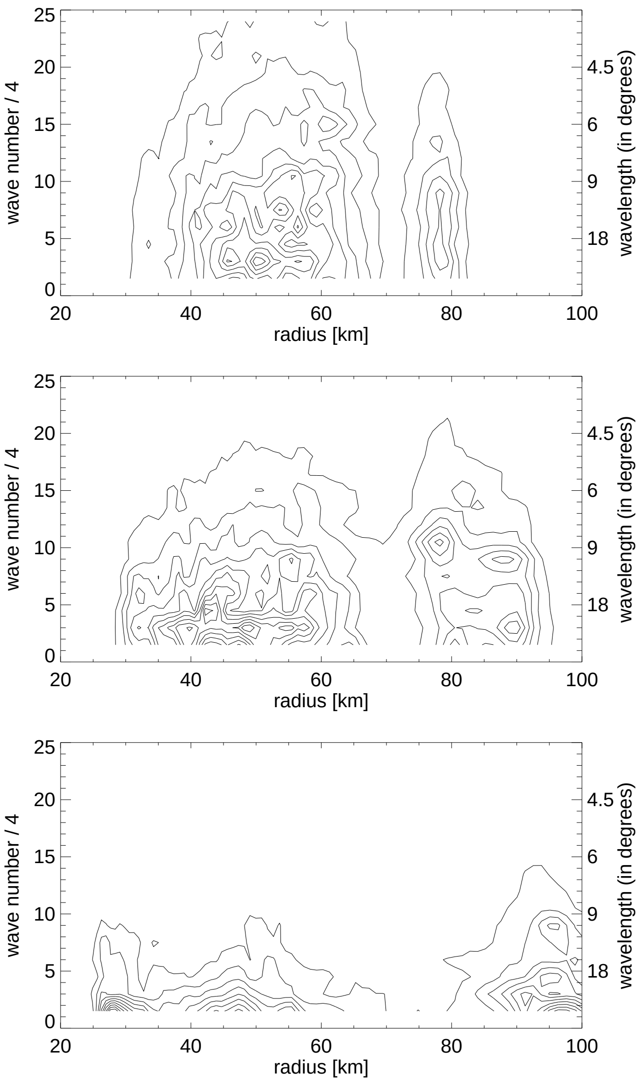

Fig. 12. Relative power of the turbulent motions at different angular scales for a three-dimensional simulation of convection inside the proto-neutron star. The simulation was performed in a wedge of opening angle 60° (between $\theta = 60°$ and $\theta = 120°$). The normal mode analysis was done with the electron fraction Y_e. The three snapshots are taken at 12.2 ms, 13.6 ms, and 16.6 ms, respectively (from top to bottom). The levels of constant power are chosen linearily in steps of 10% of the maximum value. Note that the scale on the right of each panel is nonlinear and gives the wavelength (i.e., twice the angular size) of a structure in degrees

The angular-integrated angular kinetic energy as a function of time also reveals quantitative differences between the two- and three-dimensional results (see Fig. 14). The angular kinetic energy is about a factor of 3–4 smaller in the 3D simulations than in the 2D one. Fig. 14 also shows that the angular kinetic energy in the 3D simulation performed within the 20°

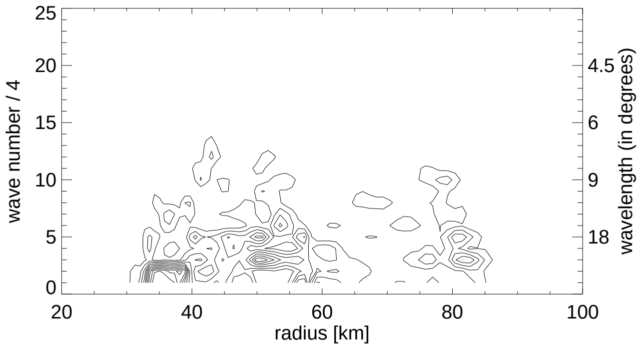

Fig. 13. Relative power of the turbulent overturn motions at different (angular) scales for a two-dimensional simulation of convection inside the proto-neutron star as deduced from the electron concentration. The snapshot is taken at 13.9 ms. The levels of constant power are chosen linearly in steps of 10% of the maximum value. Note that the scale on the right is nonlinear and gives the wavelength (i.e., twice the angular size) of a structure in degrees

sector is significantly reduced compared to the 3D simulation performed within the 60° sector. This reduction of the angular kinetic energy is caused by the insufficient angular extent of the computational domain, which hampers the development of the convective instability, because the dominant structures have wavelengths of about 20°–30° which are too large to be correctly modelled in a 20° sector. Note that early on in the evolution ($t \lesssim 14$ ms), when the dominant structures still have a small angular size, the angular kinetic energy of both 3D simulations agrees very well.

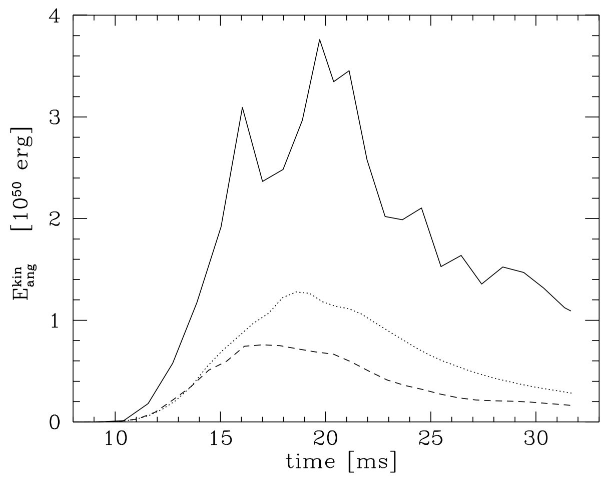

Fig. 14. Angular-integrated angular kinetic energy as a function of time: solid (2D simulation); dotted (3D simulation in a 60° sector); dashed (3D simulation in a 20° sector)

Further quantitative differences are found when comparing the root mean squared angular velocity

$$v_{\rm ang}^{\rm rms} \equiv \sqrt{\langle v_\theta^2 \rangle + \langle v_\phi^2 \rangle} \tag{3}$$

of the 2D and 3D simulations at a given epoch. Fig. 15 shows that in the three-dimensional simulations $v_{\rm ang}^{\rm rms}$ is roughly a factor of two smaller than in the two-dimensional simulation. Moreover, in 2D $v_{\rm ang}^{\rm rms}$ shows larger variations as a function of the enclosed mass than in the 3D case. This is simply caused by the fact that the 2D convective structures are twice as large and have 3–4 times more specific angular kinetic energy than the 3D ones. Hence, in the two-dimensional simulation the flow quantities are more inhomogeneous and show larger spatial fluctuations. Compared to the result of the 3D simulation with the 60° sector, the root mean squared angular velocity obtained in the 3D simulation with the 20° angular sector turns out to be smaller in the unstable region where initially both the lepton and the entropy gradient are negative. As discussed before, this is a numerical artifact of the insufficiently large angular grid in case of the simulation performed with the 20° cone.

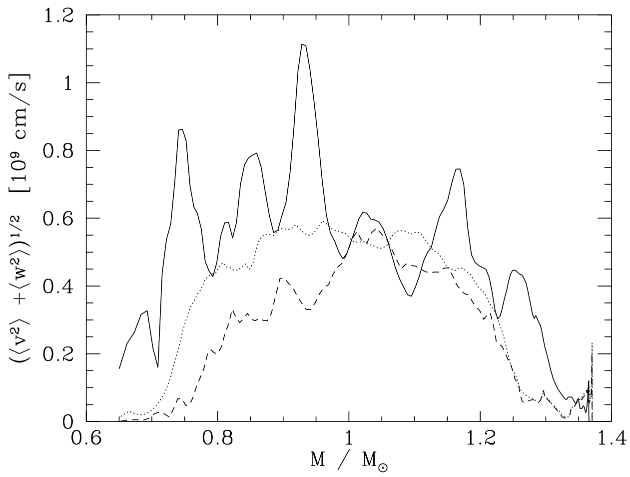

Fig. 15. Root mean squared angular velocity versus enclosed mass 18 ms after the start of the simulations: solid (2D simulation); dotted (3D simulation in a 60° sector); dashed (3D simulation in a 20° sector)

Because the root mean squared angular velocity and the angular size of the structures is smaller in the three-dimensional simulations than in the two-dimensional models, the genuine three-dimensional finger-like and blob-like structures have less momentum than their two-dimensional counterparts. This explains why in the 3D simulations the extent of undershooting at the inner edge of the convectively unstable layer is reduced compared to the undershooting found in the 2D simulation (see Fig. 16). Note that the "reference" Y_e distribution, which is displayed as the solid curve in Fig. 16 and which all multi-dimensional simulations are compared with, refers to the result of a one-dimensional simulation which leaves the initial Y_e distribution (as function of the enclosed mass) unchanged due to the disregard of neutrinos in the hydrodynamical simulation and the lack of convective mixing in the 1D case.

In two spatial dimensions convection penetrates by means of undershooting about 1.2 pressure scale heights into the adjacent convectively stable layers. In three spatial dimensions the undershooting is reduced to about 0.8 pressure scale heights, i.e., the depth of the undershooting region is smaller by about 50% than in the axisymmetrical models. Because of the insufficiently large angular grid in the 3D simulation performed with the 20° sector, the extent of undershooting is less strong by another 10 to 20% in this case (Fig. 16).

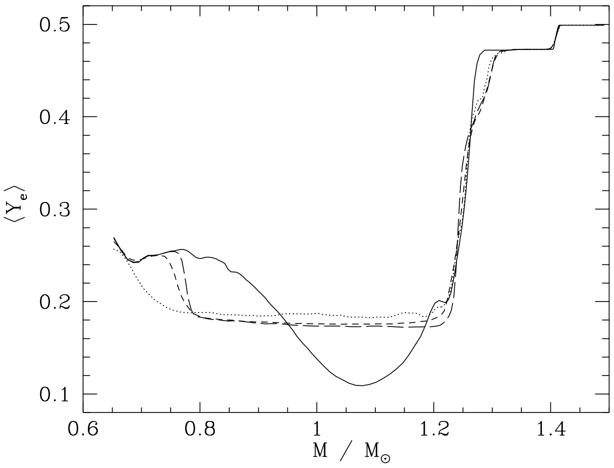

Fig. 16. Angular-averaged electron number fraction $\langle Y_e \rangle$ plotted versus enclosed mass for different simulations at 32 ms after the start of the computations: solid (1D); dotted (2D); short-dashed (3D with 60° sector); long-dashed (3D with 20° sector)

The effect of convective overturn and mixing on the density stratification and on the shock propagation is illustrated in Fig. 17, which shows the density and mass distributions at t = 32 ms for the 1D, 2D and 3D simulations. One notices that the result for the 3D case lies in between the 1D and 2D results and that in two spatial dimensions the structural effects are largest. As already mentioned above, along with the convective overturn of the matter potential energy is liberated in the multi-dimensional simulations, which drives a re-expansion of the stalled shock wave. Hence, the shock is located at larger radii in the 2D and 3D simulations than in the 1D model. Consequently, the mass distribution at small radii is more compact in the multi-dimensional cases, i.e., more mass is located inside a radius of about 45 km than in the spherically symmetrical model (Fig. 17). Compared to the 2D model these effects are reduced in the 3D simulation, because the undershooting is weaker. Therefore the mass region involved in the mixing is smaller and the proto-neutron star becomes less compact, which in turn leads to less potential energy release and to a less strong re-expansion of the shock wave, $r_{\rm sh}^{\rm 1D} \approx 220$ km $< r_{\rm sh}^{\rm 3D} \approx 280$ km $< r_{\rm sh}^{\rm 2D} \approx 400$ km at t = 32 ms, $r_{\rm sh}$ being the shock radius.

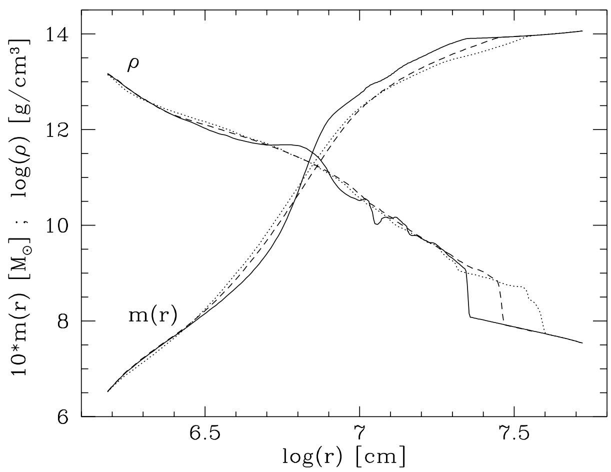

Fig. 17. Angular-averaged density and integral mass distribution 32 ms after the start of the simulations: solid (1D simulation); dotted (2D simulation); dashed (3D simulation in a 60° sector). Note the dependence of the shock position and of the compactness of the proto-neutron star on the spatial dimension of the simulation

2.2. Convection in the hot-bubble region

We have performed a second set of simulations, which were aimed at studying the convective instability in the hot-bubble region and which included a simple, but nevertheless reasonably well justified treatment of neutrino effects in the stellar matter (for details, see Janka & Müller 1995a, 1996).

In these simulations the inner part of the collapsed stellar core slightly inside the neutrinosphere was cut out and time-dependent neutrino fluxes were imposed at this inner boundary. Thereby, the neutrino emission from the central part of the proto-neutron star was mimiced. The radius of the inner boundary was either kept fixed, or was allowed to shrink with time to take into account the contraction of the cooling neutron star.

Due to neutrino heating an unstable entropy gradient builds up between the shock and the neutrinosphere. Depending on the imposed neutrino flux at the inner boundary, this hot-bubble region becomes convective after about 50–80 ms. Thus, in our second set of simulations two convective regions are present: (i) the lepton and entropy unstable layer inside the proto-neutron star just below the neutrinosphere, and (ii) the entropy-unstable hot-bubble region (see Table 1). Although we located the inner boundary somewhat inside the neutrinosphere, our computational domain did only partially encompass the convectively unstable layer in the proto-neutron star. Putting the inner boundary deeper inside the star reduces the time step appreciably and thus makes the simulation significantly more expensive, and, in particular, would have made the long time (up to 1 s past core bounce) hot-bubble simulations discussed in Janka & Müller (1995a, 1996) impracticable.

Because only part of the inner convection zone is included in the simulations the radial extent of the convective eddies and of the undershooting is constrained and suppressed by the imposed inner boundary condition. Convection inside the proto-neutron star is therefore weaker in these models than we would expect in simulations without an inner boundary at finite radius. Hence, the gravitational waves produced by anisotropies in these models are primarily caused by non-radial motions in the hot-bubble region (see Sect. 3).

The initial model was the collapsed 1.31 $M_\odot$ iron core of a 15 $M_\odot$ star at a time about 25 ms after core bounce. By that time the prompt shock wave had transformed into a standing accretion shock at a radius of about 115 km, enclosing a mass of 1.25 $M_\odot$. The matter behind the shock has small negative velocities and settles onto the forming neutron star. The initial model was provided by Bruenn (private communication; see also Bruenn 1993).

The two-dimensional simulations of convection in the hot-bubble region were performed in spherical coordinates. The computational grid consisted of 400 radial zones distributed non-equidistantly between the time-dependent inner boundary and the fixed outer edge of the grid at 17000 km, with 100 radial zones out to 290 km and 42 radial zones within the innermost 100 km. Initially the inner boundary was located at 31.7 km ($\rho = 1.7 \times 10^{12}$ g/cm^3) with an interior mass (constant in time) of 0.848 $M_\odot$. Over a period of about 0.5 s the radius of the inner boundary was reduced to a value of 15 km. Thereby, we have simulated the contraction of the proto-neutron star due to lepton and energy losses. The gravitational potential was computed in the same way as in the 2D simulations of convection inside the proto-neutron star, i.e., as the superposition of contributions from the spherically symmetrical point-mass potential associated with the mass inside the inner boundary and from the 2D matter distribution in the computational domain. In angular direction between 90 and 180 equidistant zones were used. In all simulations axial symmetry was assumed, and in some simulations, in addition, equatorial symmetry was imposed. The latter restriction was found, however, to influence the growth of large-scale ($\gtrsim 30°$) angular modes negatively (for more details see Janka & Müller 1995a, 1996)

3. Gravitational wave signature

The non-radial motions and the resulting time-dependence and asphericities of the density stratification due to convection in the unstable layers both inside the proto-neutron star and in the neutrino-heated hot-bubble will produce gravitational radiation. Thus, we have analysed the two- and three-dimensional models discussed in the previous section and have computed the amount and the signature of gravitational radiation that can be expected from convection in Type II supernovae. Moreover, the density and temperature variations in the neutrino-decoupling region (see Fig. 7) and the fast convective overturn below the neutrinosphere lead to anisotropies of the neutrino emission which will also be a source of gravitational waves (Epstein 1978, Turner 1978).

3.1. Formalism

The gravitational wave signal was calculated using a post-Newtonian approach, where numerically troublesome higher order time derivatives of the quadrupole moment are transformed into much better tractable spatial derivatives. In particular, for the gravitational quadrupole radiation field, $h^{\rm TT}$, we used an expression derived independently by Nakamura & Oohara (1989), and by Blanchet et al. (1990):

$$\begin{aligned} h^{\rm TT}_{ij}(\boldsymbol{X},t) &= \frac{2G}{c^4 R} P_{ijkl}(\boldsymbol{N}) \times \\ &\times \int {\rm d}^3x\, \rho \left[2v^k v^l - x^k\, \partial_l \Phi - x^l\, \partial_k \Phi \right] , \end{aligned} \tag{4}$$

where $R = |\boldsymbol{X}|$ is the distance between the observer and the source, Φ is the Newtonian gravitational potential, ρ is the mass-density and $\boldsymbol{v}$ is the velocity. The other quantities have their usual meaning except for $P_{ijkl}(\boldsymbol{N})$ (with $\boldsymbol{N} = \boldsymbol{X}/R$) which denotes the transverse-traceless (TT) projection operator onto the plane orthogonal to the outgoing wave direction $\boldsymbol{N}$, acting on symmetrical Cartesian tensors according to

$$\begin{aligned} P_{ijkl}(\boldsymbol{N}) &= (\delta_{ik} - N_i N_k)\,(\delta_{jl} - N_j N_l) + \\ &- \frac{1}{2}(\delta_{ij} - N_i N_j)\,(\delta_{kl} - N_k N_l)\,. \end{aligned} \tag{5}$$

∂_i represents the partial derivative with respect to the x^i coordinate. The integrand in Eq. (4) is defined on a compact manifold and is known to the (2nd order) accuracy level of the numerical algorithm of the hydro-code. Eq. (4) can be shown to be equivalent to the standard representation

$$h^{\rm TT}_{ij}(\boldsymbol{X},t) = \frac{2G}{c^4 R}\, P_{ijkl}(\boldsymbol{N})\, \frac{\partial^2}{\partial t^2} Q_{kl}\, (t - \frac{R}{c}) \tag{6}$$

where the trace-free part of the mass-quadrupole tensor of the matter distribution is given by

$$Q_{ij}(t) = \int {\rm d}^3x\, \rho(\boldsymbol{x},t)\, \left(x_i x_j - \frac{1}{3}\delta_{ij}\boldsymbol{x}^2 \right)\,. \tag{7}$$

It can easily be shown that evaluating the integral of Eq. (4) by an integration scheme (of at least 2nd order) is by one order of accuracy superior to twice applying numerical time-differentiation methods to quadrupole data given at discrete points of time (see Mönchmeyer et al. 1991).

3.1.1. Evaluation in two dimensions

The gravitational radiation field gives direct information about the second time derivative of the mass-quadrupole tensor (see Eq. (7)). In case of axisymmetry the quadrupole moment, Q, is the only independent component of the quadrupole tensor. Its relation to the Cartesian components Q_{ij} of the radiative mass-quadrupole tensor is

$$Q \equiv \frac{3}{4}\sqrt{\frac{5}{\pi}}\, Q_{zz}\,. \tag{8}$$

As all our simulations were performed in spherical coordinates, it is natural to represent the (total) radiation field $\widetilde{h}^{\mathrm{TT}}$ in terms of the "pure-spin tensor harmonics" $T_{ij}^{\mathrm{E2},lm}$ and $T_{ij}^{\mathrm{B2},lm}$ with amplitudes A_{lm}^{E2} and A_{lm}^{B2} in the following way (Thorne 1980):

$$\widetilde{h}_{ij}^{\mathrm{TT}}(\boldsymbol{X},t) = \frac{1}{R}\sum_{l=2}^{\infty}\sum_{m=-l}^{+l}\left\{ A_{lm}^{\mathrm{E2}}(t-\frac{R}{c})\,T_{ij}^{\mathrm{E2},lm}(\theta,\phi) + A_{lm}^{\mathrm{B2}}(t-\frac{R}{c})\,T_{ij}^{\mathrm{B2},lm}(\theta,\phi)\right\}. \quad (9)$$

For the definitions of $T_{ij}^{\mathrm{E2},lm}$, $T_{ij}^{\mathrm{B2},lm}$, A_{lm}^{E2}, and A_{lm}^{B2}, see Thorne (1980). In spherical coordinates the coefficients A_{lm}^{E2} and A_{lm}^{B2} have especially simple integral representations over the source. By symmetry, there is only one nonvanishing quadrupole term in Eq. (9), namely A_{20}^{E2}. Higher-order terms are neglected in the quadrupole approximation h^{TT} of the gravitational radiation field $\widetilde{h}^{\mathrm{TT}}$. Transforming Eq. (4) to spherical coordinates and expressing v_i in terms of unit vectors in the r, θ and ϕ direction, one obtains by comparison of Eq. (4) with the lowest-order term of Eq. (9) for the quadrupole wave amplitude A_{20}^{E2} the expression

$$\begin{aligned} A_{20}^{\mathrm{E2}}(t) \;=\; & \frac{G}{c^4}\frac{32\pi^{3/2}}{\sqrt{15}}\int_0^1\int_0^{\infty}\varrho(r,z,t)\Big[v_r v_r(3z^2-1) + \\ & + v_\theta v_\theta(2-3z^2) - v_\phi v_\phi - 6 v_r v_\theta z\sqrt{1-z^2} + \\ & - r\partial_r\Phi(3z^2-1) + 3\partial_\theta\Phi z\sqrt{1-z^2}\Big] r^2 \mathrm{d}r\mathrm{d}z\ , \end{aligned} \quad (10)$$

where $\partial_r = \partial/\partial r$, $\partial_\theta = \partial/\partial\theta$, and $z = \cos\theta$.

From the definition of $T_{ij}^{\mathrm{E2},2m}$ (Thorne 1980, Eq. (2.39e)) one derives for the components of h^{TT} the formula

$$h_{\theta\theta}^{\mathrm{TT}} = \frac{1}{8}\sqrt{\frac{15}{\pi}}\,\sin^2\theta\,\frac{A_{20}^{\mathrm{E2}}(t)}{R}\ . \quad (11)$$

The only other nonzero component is $h_{\phi\phi}^{\mathrm{TT}} = -h_{\theta\theta}^{\mathrm{TT}}$. The total energy radiated in gravitational waves is then given by the general expression

$$E = \frac{c^3}{G}\frac{1}{32\pi}\sum_{l,m}\int_{-\infty}^{+\infty}\left\{\left(\frac{\mathrm{d}A_{lm}^{\mathrm{E2}}}{\mathrm{d}t}\right)^2 + \left(\frac{\mathrm{d}A_{lm}^{\mathrm{B2}}}{\mathrm{d}t}\right)^2\right\}\mathrm{d}t\ . \quad (12)$$

The total energy radiated per unit frequency will be denoted by $\mathrm{d}E/\mathrm{d}\nu$ and was calculated by interpolating the data for the amplitudes A_{20}^{E2} that are given at non-equidistant times onto an equidistant temporal grid and using the fast Fourier transform technique with a rectangular window function.

3.1.2. Evaluation in three dimensions

If the source is of genuine three-dimensional nature, it is common to express the gravitational quadrupole radiation field, h^{TT}, in the following tensorial form (see, e.g., Misner et al. 1973)

$$h_{ij}^{\mathrm{TT}}(\boldsymbol{X},t) = \frac{1}{R}\left(A_+ \boldsymbol{e}_+ + A_\times \boldsymbol{e}_\times\right) \quad (13)$$

with the unit linear-polarization tensors

$$\boldsymbol{e}_+ \;=\; \boldsymbol{e}_\theta\otimes\boldsymbol{e}_\theta - \boldsymbol{e}_\phi\otimes\boldsymbol{e}_\phi\ , \quad (14)$$
$$\boldsymbol{e}_\times \;=\; \boldsymbol{e}_\theta\otimes\boldsymbol{e}_\phi + \boldsymbol{e}_\phi\otimes\boldsymbol{e}_\theta\ , \quad (15)$$

$\boldsymbol{e}_\theta$ and $\boldsymbol{e}_\phi$ being the unit polarization vectors in θ and ϕ-direction of a spherical coordinate system and $\otimes$ the tensor product. The amplitudes A_+ and $A_\times$ represent the only two independent modes of polarization in the TT gauge, and are given by the following expressions for $\theta = 0, \phi = 0$

$$A_+ \;=\; \ddot{I}_{xx} - \ddot{I}_{yy}\ , \quad (16)$$
$$A_\times \;=\; 2\ddot{I}_{xy}\ , \quad (17)$$

and for $\theta = \pi/2, \phi = 0$ by

$$A_+ \;=\; \ddot{I}_{zz} - \ddot{I}_{yy}\ , \quad (18)$$
$$A_\times \;=\; -2\ddot{I}_{yz}\ , \quad (19)$$

where

$$\ddot{I}_{ij} = \frac{G}{c^4}\int \mathrm{d}^3x\,\rho\,\left(2v_i v_j - x_i\partial_j\Phi - x_j\partial_i\Phi\right)\ . \quad (20)$$

The total energy radiated in form of gravitational waves is then given by

$$E \;=\; \frac{c^3}{5G}\int_{-\infty}^{+\infty}\left[\frac{\mathrm{d}}{\mathrm{d}t}\Big(A_{ij} - \frac{1}{3}\delta_{ij}A_{ll}\Big)\right]^2\,\mathrm{d}t \quad (21)$$
$$\begin{aligned} \;=\; & \frac{2c^3}{15G}\int_{-\infty}^{+\infty}\big[\dot{A}_{xx}^2 + \dot{A}_{yy}^2 + \dot{A}_{zz}^2 - \dot{A}_{xx}\dot{A}_{yy} - \dot{A}_{xx}\dot{A}_{zz} + \\ & - \dot{A}_{yy}\dot{A}_{zz} + 3\,(\dot{A}_{xy}^2 + \dot{A}_{xz}^2 + \dot{A}_{yz}^2)\big]\ \mathrm{d}t \end{aligned} \quad (22)$$

with

$$A_{ij} \;\equiv\; \ddot{I}_{ij}\ . \quad (23)$$

3.1.3. Gravitational waves from neutrino emission

In order to estimate the gravitational wave signal associated with the anisotropic emission of neutrinos, we use Eq. (16) of Epstein (1978) in the limit of a very distant source, $R = |\boldsymbol{X}| \to \infty$. In addition, we make use of the approximation that the gravitational wave signal measured by an observer at time t is caused only by radiation emitted at time $t' = t - R/c$. Hence, we take $t - t' = \mathrm{const} = R/c$, which means that only a neutrino pulse itself is assumed to cause a gravitational wave signal but memory effects after the pulse has passed the observer are disregarded. With these simplifications, one gets for the dimensionless gravitational wave amplitude

$$h_{ij}^{\mathrm{TT}}(\boldsymbol{X},t) \;=\; \frac{4G}{c^4R}\int_{-\infty}^{t-R/c}\mathrm{d}t' \int_{4\pi}\mathrm{d}\Omega'\,\frac{\left(n_i n_j\right)^{\mathrm{TT}}}{1-\cos\theta}\cdot\frac{\mathrm{d}L_\nu(\boldsymbol{\Omega}',t')}{\mathrm{d}\Omega'} \quad (24)$$

with θ being the angle between the direction towards the observer and the direction $\mathbf{\Omega}'$ of the radiation emission, and $\mathrm{d}L_\nu(\mathbf{\Omega}, t)/\mathrm{d}\Omega$ denoting the direction dependent neutrino luminosity, i.e., the energy radiated at time t per unit of time and per unit of solid angle into direction $\mathbf{\Omega}$. The angular integral over the radiation source is performed over $\mathrm{d}\Omega' = -\mathrm{d}(\cos\vartheta')\mathrm{d}\varphi'$ and thus over all angles ϑ' and φ' which specify the (beam) direction in the source coordinate frame (x', y', z') that we identify with the coordinate frame used for the hydrodynamical simulations. With the angles θ and ϕ defining the radiation direction in the observer's frame (x, y, z) (where the observer is located at distance R along the z-axis) one has $(n_x n_x)^{\mathrm{TT}} = \frac{1}{2}\left(1-\cos^2\theta\right)\left(2\cos^2\phi - 1\right) = \frac{1}{2}\left(1-\cos^2\theta\right)\cos(2\phi)$, and the gravitational wave amplitude is given by

$$h^{\mathrm{TT}}_{xx} = -h^{\mathrm{TT}}_{yy} = -h^{\mathrm{TT}}_{+} = = \frac{2G}{c^4 R}\int_{-\infty}^{t-R/c} \mathrm{d}t' \int_{4\pi} \mathrm{d}\Omega' \; (1+\cos\theta)\cos(2\phi)\,\frac{\mathrm{d}L_\nu(\mathbf{\Omega}', t')}{\mathrm{d}\Omega'} \,. \tag{25}$$

Replacing $\cos(2\phi)$ by $\sin(2\phi)$ in Eq. (25) yields $h^{\mathrm{TT}}_{xy} = h^{\mathrm{TT}}_{\times}$.

In Eq. (25) θ and ϕ need to be expressed in terms of the angles ϑ', φ', ϑ, and φ when ϑ and φ define the orientation of the observer's coordinate system (observer located in z-direction and y-axis lying in the x'-y'-plane) relative to the source coordinate frame. Choosing $\varphi = 0$ the y- and y'-axes coincide and the expressions become rather simple. For $\vartheta = 0$ the z-axis and the z'-axis are identical, too, and the observer is situated along the system's z'- (polar) axis. In that case one obtains

$$\left(h^{\mathrm{TT}}_{xx}\right)_{\mathrm{p}} = \frac{2G}{c^4 R}\int_{-\infty}^{t-R/c} \mathrm{d}t' \int_{4\pi} \mathrm{d}\Omega' \; \left(1+\cos\vartheta'\right)\cos(2\varphi')\,\frac{\mathrm{d}L_\nu(\mathbf{\Omega}', t')}{\mathrm{d}\Omega'} \,. \tag{26}$$

When $\mathrm{d}L_\nu/\mathrm{d}\Omega$ is axially symmetrical, the gravitational wave signal for an observer on the symmetry axis vanishes and $\left(h^{\mathrm{TT}}_{xx}\right)_{\mathrm{p}} = 0$. For $\vartheta = \pi/2$ the observer is positioned perpendicular to the source's z'-axis in the equatorial plane (z-axis and x'-axis coincide) and h^{TT}_{xx} becomes

$$\left(h^{\mathrm{TT}}_{xx}\right)_{\mathrm{e}} = \frac{2G}{c^4 R}\int_{-\infty}^{t-R/c} \mathrm{d}t' \int_{4\pi} \mathrm{d}\Omega' \; \left(1+\sin\vartheta'\cos\varphi'\right)\frac{\cos^2\vartheta' - \sin^2\vartheta'\sin^2\varphi'}{\cos^2\vartheta' + \sin^2\vartheta'\sin^2\varphi'} \times \frac{\mathrm{d}L_\nu(\mathbf{\Omega}', t')}{\mathrm{d}\Omega'} \,. \tag{27}$$

Equations (26) and (27) can be rewritten as

$$h^{\mathrm{TT}}_{xx} = \frac{2G}{c^4 R}\int_{-\infty}^{t-R/c} \mathrm{d}t' \; L_\nu(t')\cdot\alpha(t') \tag{28}$$

with the anisotropy parameter $\alpha(t)$ being defined by

$$\alpha(t) \equiv \frac{1}{L_\nu(t)}\cdot\int_{4\pi} \mathrm{d}\Omega' \; \Psi(\vartheta', \varphi')\cdot\frac{\mathrm{d}L_\nu(\mathbf{\Omega}', t)}{\mathrm{d}\Omega'} \tag{29}$$

where $\Psi(\vartheta', \varphi')$ denotes the angle dependent factors appearing in the integrals of Eqs. (26) and (27), respectively, and $L_\nu(t)$ is the total neutrino luminosity,

$$L_\nu(t) = \int_{4\pi} \mathrm{d}\Omega' \; \frac{\mathrm{d}L_\nu(\mathbf{\Omega}', t)}{\mathrm{d}\Omega'} \,. \tag{30}$$

Using the dimensionless gravitational wave amplitude of Eq. (29) and taking into account that there is only one non-zero component of the quadrupole amplitude, Eqs. (11) and (12) allow one to estimate the total energy $E(t)$ that is associated with the gravitational waves produced by the anisotropic emission of neutrinos in the two-dimensional (axially symmetrical) case until time t:

$$E(t) = \beta\cdot\frac{G}{c^5}\int_{-\infty}^{t-R/c} \mathrm{d}t' \; L^2_\nu(t')\cdot\alpha^2(t') \,. \tag{31}$$

β is a numerical factor of order unity, typically around 0.5. Employing Eq. (13) and Eqs. (16)–(23) and assuming that all amplitudes A_{ij} contribute roughly equally, one finds that Eq. (31) also holds for the three-dimensional situation but with a slightly different value of β.

3.2. Two-dimensional results

The results of our gravitational wave analysis for four different models are displayed in Figs. 18 to 21 which show the quadrupole wave amplitudes, the quadrupole amplitude spectra, the spectral energy densities, and the energies radiated in form of gravitational waves, respectively. One first notices that the signal forms and signal strengths as well as the spectral distributions of the gravitational wave energy depend on whether the gravitational radiation is produced by convection inside the proto-neutron star or by convection in the hot-bubble region. Generally speaking, in case of convective overturn processes in the proto-neutron star, the maximum gravitational wave amplitude is significantly larger ($\approx$ 700 cm instead of $\lesssim$ 100 cm), the spectral energy distribution is peaked at higher frequencies (at 500 Hz to 1000 Hz instead of at about 100 Hz), and much more energy is radiated in form of gravitational waves ($2\times10^{-9}\,M_\odot c^2$ instead of $\lesssim 10^{-12}\,M_\odot c^2$) as compared to multi-dimensional processes in the hot-bubble region.

In model HB2D, which refers to the two-dimensional simulation of convection inside the proto-neutron star starting with Hillebrandt's configuration of a post-bounce stellar core, the strongly unstable lepton and entropy gradients give rise to large convective velocities which exceed 10^9 cm/s and are hence transonic. As the unstable layer involves a relatively large amount of mass ($\approx 0.45 - 0.5\,M_\odot$) the angular kinetic energy of the convective flow is substantial ($E^{\mathrm{ang}}_{\mathrm{kin}} \lesssim 3.8\times10^{50}$ erg). Moreover, because of the compact and quite massive collapsed stellar core (1.4 $M_\odot$) in model HB2D the non-radial flow takes place deep in a strong gravitational potential with convective elements undershooting the stable layer down to a radius of about 15 km. Consequently, this model produces a relatively strong gravitational wave signal with a maximum amplitude of

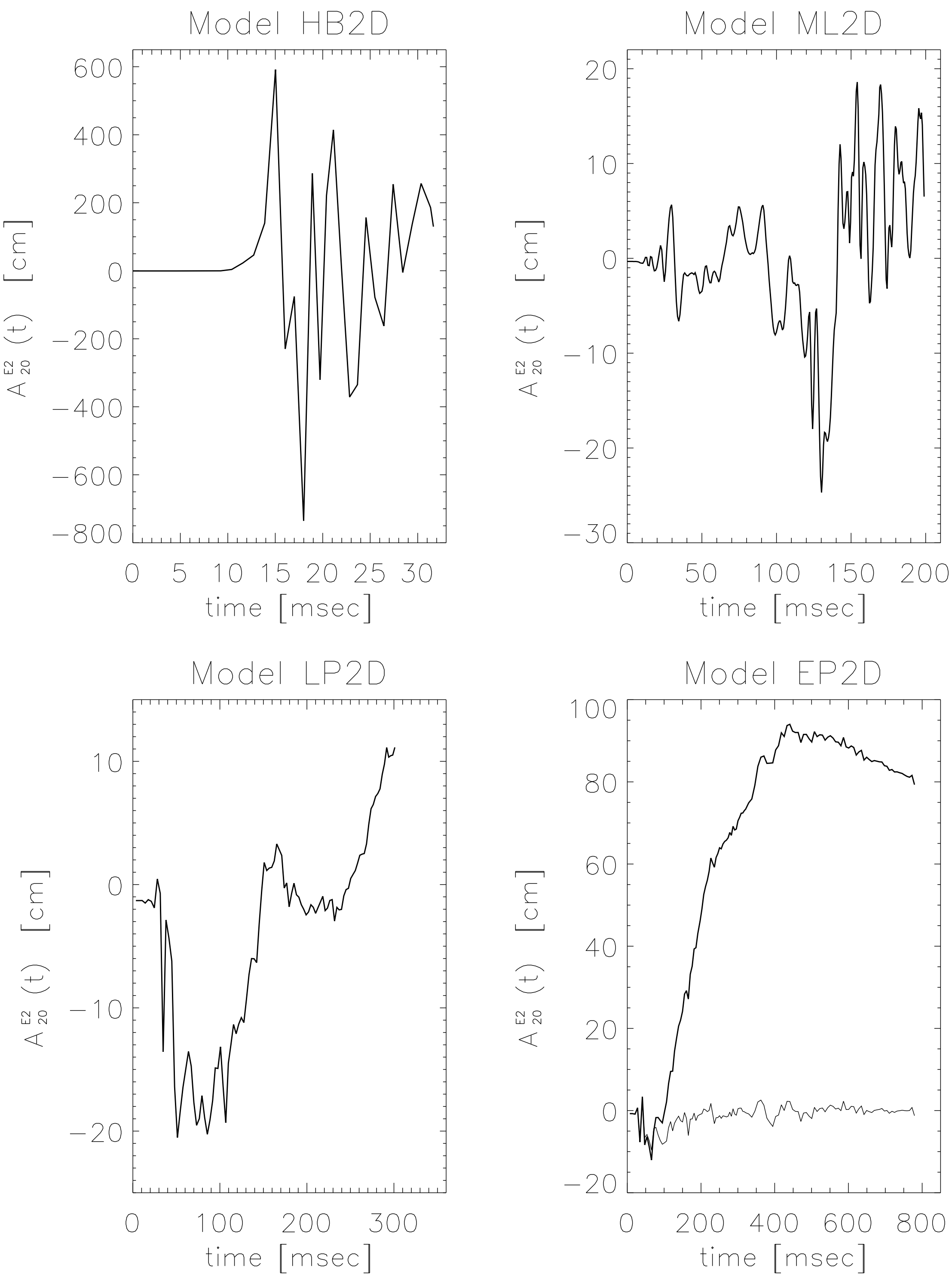

Fig. 18. Quadrupole amplitude A^{E2}_{20} [cm] of various models versus time. The upper left panel shows the amplitude obtained from a two-dimensional simulation of convection inside the proto-neutron star (see Sect. 2.1). The remaining three panels give the amplitudes obtained from two-dimensional simulations of convection in the hot-bubble region. The initial neutrino flux imposed at the inner boundary increases along the model sequence ML2D (top right), LP2D (bottom left), and EP2D (bottom right) from $L^0_{\nu_e} = 2.0 \times 10^{52}$ erg/s to $L^0_{\nu_e} = 2.25 \times 10^{52}$ erg/s (see Janka & Müller 1996), leading to increasingly faster explosions and higher supernova explosion energies (0.5×10^{51}, 1.1×10^{51}, and 1.3×10^{51} erg, respectively). The additional thin curve in the lower right panel gives the quadrupole amplitude produced by the convection inside the proto-neutron star alone. It is very small in models ML2D, LP2D, and EP2D because the convectively unstable region inside the proto-neutron star was only partially included in these simulations

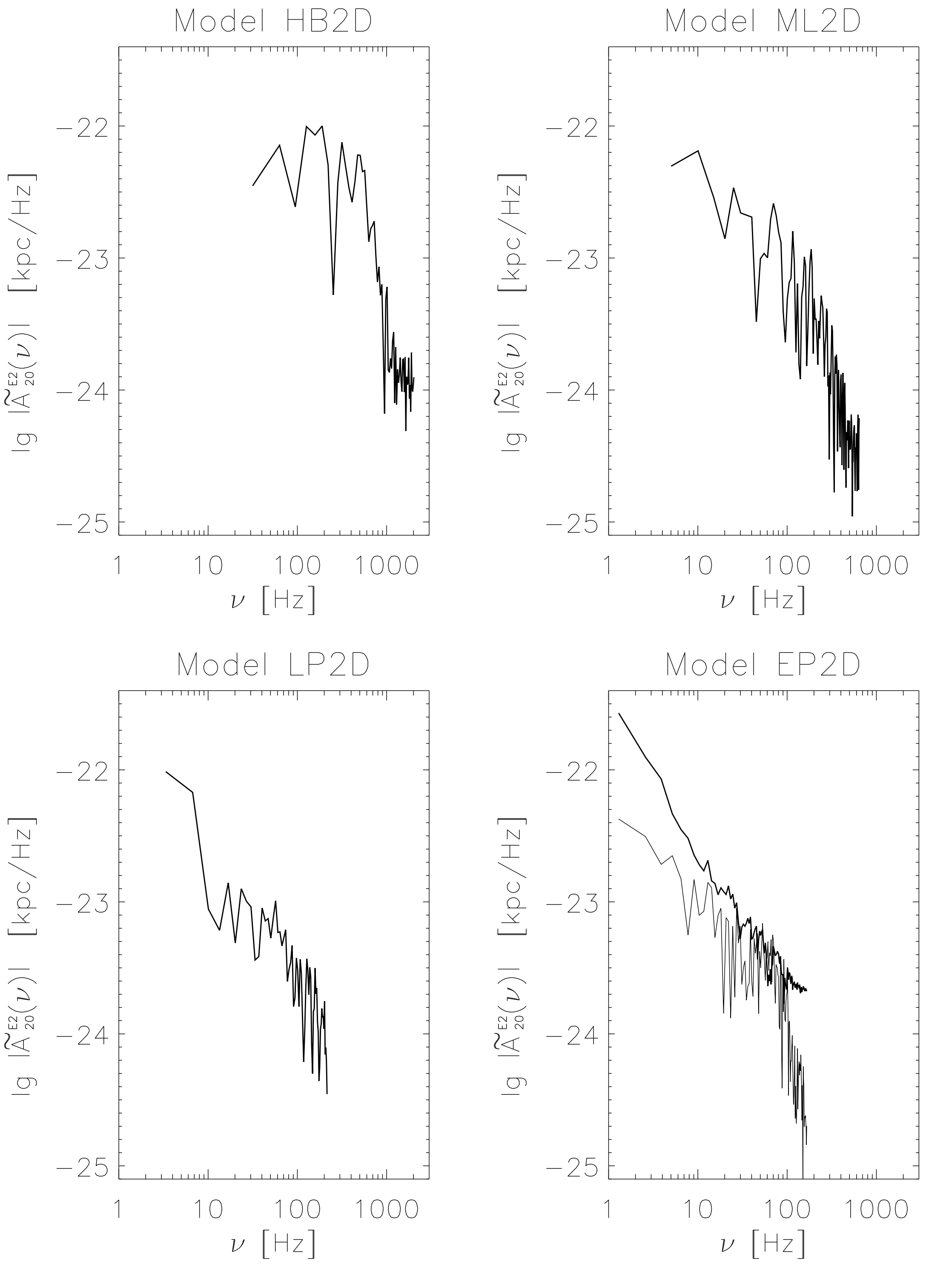

Fig. 19. Similar to Fig. 18 but showing the quadrupole amplitude spectra $|\widetilde{A}^{E2}_{20}(\nu)|$ [kpc/Hz] as a function of the frequency of the emitted gravitational radiation

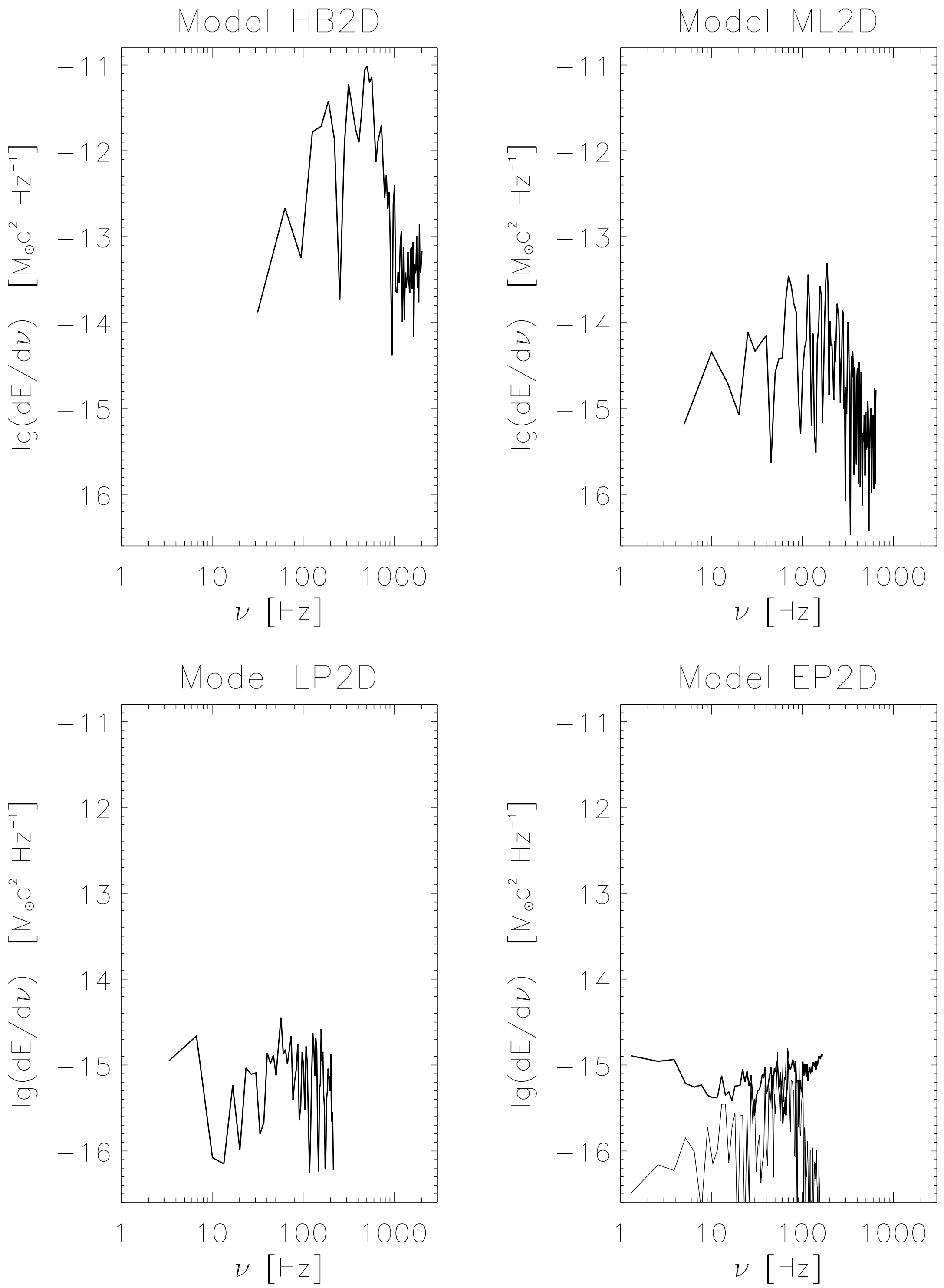

Fig. 20. Similar to Fig. 18 but showing the spectral energy density $\mathrm{d}E(\nu)/\mathrm{d}\nu$ [$M_{\odot}c^2$/Hz] of the quadrupole radiation as a function of the frequency of the emitted gravitational radiation

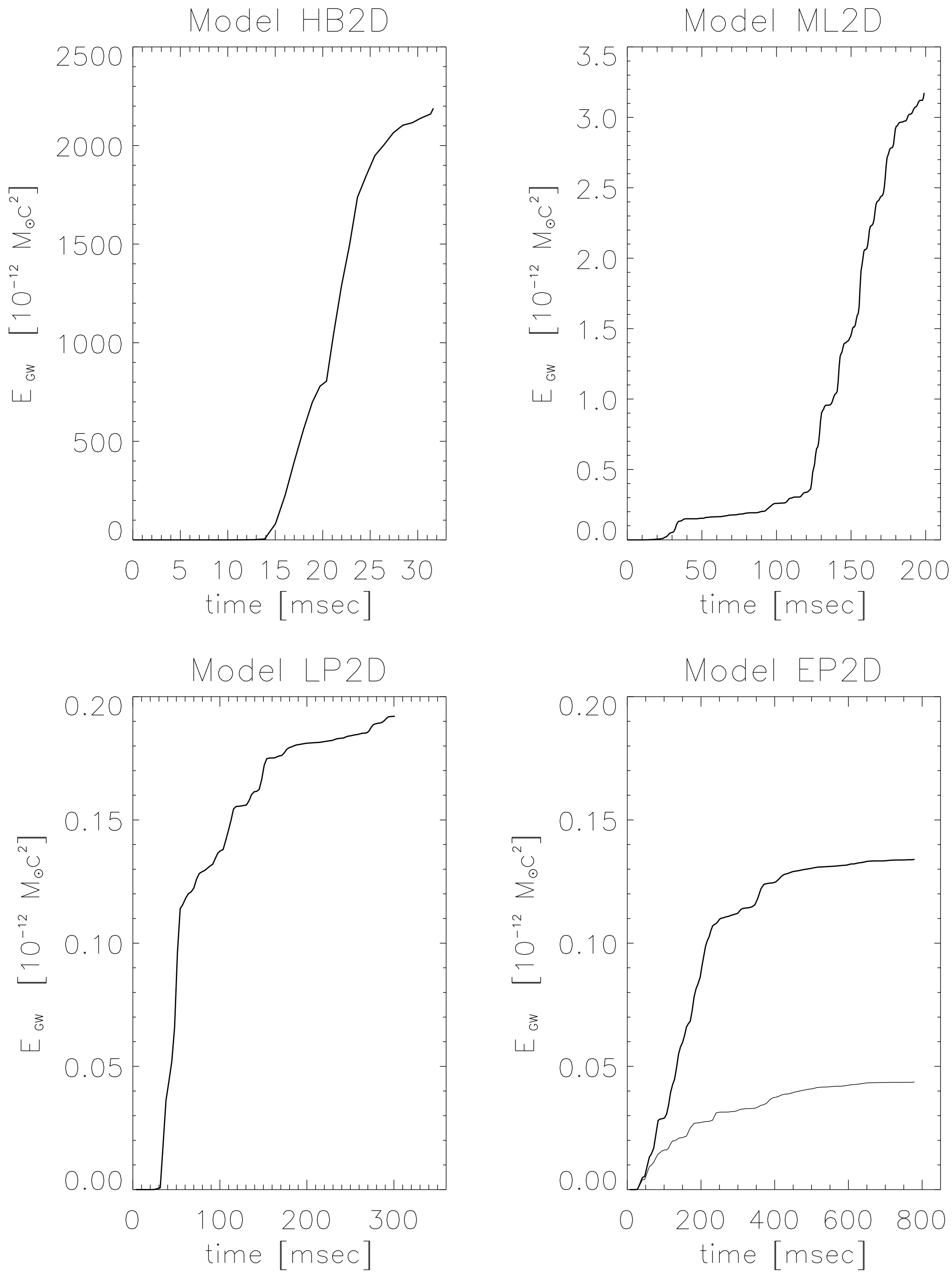

Fig. 21. Similar to Fig. 18 but showing the energy radiated in form of gravitational waves $E_{\rm GW}$ $[10^{-12}\ M_{\odot}c^2]$ as a function of time

$|A_{20}^{\rm E2}| = 735$ cm (Fig. 18) and a total emitted gravitational wave energy of $E_{\rm GW} = 2.2 \times 10^{-9}\ M_\odot c^2$ (Fig. 21). Corresponding to the characteristic overturn timescales of the convective eddies of about 2–10 ms, the frequency spectrum of the quadrupole amplitude has a broad maximum at about 100–500 Hz (Fig. 19) and the energy spectrum shows most power being radiated between 100 and roughly 1000 Hz (Fig. 20).

As discussed in Sect. 2.2, convection inside the proto-neutron star is much weaker in those of our models which we particularly used to study convection in the hot-bubble region. There are three reasons for this. Firstly, only the outer part of the convective zone in the proto-neutron star is included in the simulations, i.e., only about $0.15\ M_\odot$ of the roughly $0.3\ M_\odot$ that are unstable against convection. Secondly, the lepton and entropy gradients in Bruenn's initial model are less unstable than those in Hillebrandt's collapsed stellar core. Thirdly, due to the smaller core mass of only about $M_{\rm core} \approx 1.3\ M_\odot$ the gravitational potential is weaker in Bruenn's model and there is less mass in the unstable layer around and below the neutrinosphere. In the hot-bubble simulations the convective velocities inside the proto-neutron star are therefore significantly smaller, only about $v_{\rm conv} \approx 2 \times 10^8$ cm/s, and, correspondingly, the angular kinetic energies reach only about $E_{\rm kin}^{\rm ang} \approx 4$–$5 \times 10^{48}$ erg at a time when the convection inside the proto-neutron star is fully developed (at $t \approx 30$ ms, compare Fig. 9 in Janka & Müller 1996). Thus, the resulting gravitational wave signal from the convective overturn inside the proto-neutron star is very weak in these models as compared to model HB2D. In fact, in the models where we followed the neutrino effects in the hot-bubble region, the gravitational wave emission is strongly dominated by the waves produced by mass motions in the neutrino-heated layer between proto-neutron star and supernova shock.

We have analysed three such models, namely models ML2D, LP2D, and EP2D (equivalent to models T2c, T3c, and T4c, respectively, in Janka & Müller 1996), whose gravitational wave signature we discuss in the following. We point out here that the actual gravitational wave signal of these models will be considerably larger if the whole convection zone inside the proto-neutron star, which yields only a minor contribution to the gravitational wave emission in the presented models, is included in the simulations. Models ML2D, LP2D, and EP2D are nevertheless useful to investigate especially the characteristics of the gravitational waves originating from turbulent motions in the hot-bubble region. We find that the structure of the produced waves contains detailed information about duration, strength, and pattern of the accretion and convection processes behind the supernova shock. When these dynamical processes have direct influence on the neutrino emission, e.g., when matter accreted onto the neutron star produces additional neutrino emission, we notice correlations of the neutrino luminosity with the gravitational wave amplitude and luminosity. Moreover, our models suggest that strength and duration of turbulent processes around the proto-neutron star are correlated with the size and temporal decay of the neutrino fluxes from the proto-neutron star and with the explosion energy of the supernova. For this reason we expect, and indeed observe, characteristic differences of the gravitational wave signature of models with different explosion dynamics and different explosion parameters.

In model ML2D the temporal modulations of the gravitational wave signal and the neutrino losses from the hot-bubble region show clear correlations (compare the upper right panel in Fig. 18 with Fig. 18 in Janka & Müller 1996). Neutrino emission and gravitational wave emission from the turbulent layers around the proto-neutron star in this model are produced by downflows of cold material from the postshock region. These narrow downflows reach very high velocities of more than twice the speed of sound and are abruptly decelerated at a radius of about 80 km (see Figs. 15 and 16 in Janka & Müller 1996). The peaks and characteristic features in the neutrino emission are associated with the dissipation of kinetic energy of the gas in the surroundings of the proto-neutron star. The aspherical, dynamical gas motions also act as source of gravitational waves. The large variations of the gravitational wave amplitude around $t \approx 120$–140 ms (Fig. 18) are directly correlated with spikes in the lepton number loss/gain rate and the energy loss/gain rate of the stellar gas at the same epoch (Fig. 18 in Janka & Müller 1996). Similarly, the variation of the gravitational wave amplitude between 150 ms and 200 ms is mirrored by a correlated activity in the lepton and energy loss/gain rates. Actually, one can observe a slight time-lag of the neutrino emission. This shift can be explained by the fact that the gravitational wave emission traces the dynamical infall of the downflows, whereas the neutrino emission peaks at the moment when the infalling gas reaches highest temperatures and densities, i.e., typically at the moment when it is decelerated and strongly compressed near the proto-neutron star. The characteristic timescale of gas motions and convective overturn in the hot-bubble region is of the order of several ten to about 100 ms. The frequency spectrum of the quadrupole amplitude therefore peaks at frequencies of about 10 to roughly 100 Hz (Fig. 19), and the energy spectrum has a maximum between 50 and 200 Hz with significant power in the frequency range from 10 to 400 Hz (Fig. 20).

The gravitational wave signal of model LP2D is characterized by the low-frequency emission from the aspherical expansion of postshock material and by the superimposed high-frequency modes that are produced by small-scale convective processes in the neutrino heated hot-bubble region. The prolate, large-scale deformation of the supernova shock leads to a time-dependent mass quadrupole moment that varies within a typical time of about 100 ms. While the effect of the expansion of supernova shock and ejecta becomes prominent in the gravitational wave signature at times later than about 100 ms after the start of the simulation, the overturn of neutrino-heated material determines the wave amplitude during the first 100 ms where signal variations on timescales of 10–20 ms are visible. The gravitational wave amplitude reaches a maximum value of $|A_{20}^{\rm E2}| = 20$ cm (Fig. 18) and has typical frequencies between about 10 and 100 Hz (Fig. 19). The energy spectrum peaks at about 50–70 Hz ((Fig. 20) and the total energy radiated in gravitational waves is $E_{\rm GW} = 1.9 \times 10^{-13}\ M_\odot c^2$ which is almost a factor of 20 smaller than in model ML2D where it is $E_{\rm GW} = 3.2 \times 10^{-12}\ M_\odot c^2$ within a similar time of 200–300 ms after supernova shock formation. While the major part of the gravitational wave emission of model ML2D is produced by anisotropic, dynamical downflows of matter from the postshock region to the proto-neutron star, roughly half of the gravitational wave energy of model LP2D results from overturn motions of neutrino-heated gas and the other half from the large-scale expansion.

In model EP2D the explosion happens faster (due to higher core neutrino fluxes) and the convective overturn in the neutrino-heated region is correspondingly shorter. The contribution of the large-scale deformation and expansion of the postshock region to the gravitational wave signal therefore clearly dominates the wave amplitude after about 100 ms (Fig. 18). On a timescale of hundreds of milliseconds the wave amplitude exhibits the slow variation associated with the change of the mass quadrupole moment due to the global dynamical evolution of the explosion. However, it shows only little substructure of higher frequencies because the rapid expansion of model EP2D limits the duration of the phase of convective overturn in the hot-bubble region to about 100 ms. This can be verified in the quadrupole amplitude spectrum (Fig. 19) which confirms the clear dominance of low-frequency modes (around 1–10 Hz) and essentially no pronounced features at higher frequencies. The corresponding energy spectrum (Fig. 20) is very flat and spans the range of frequencies between about 1 Hz and roughly 100 Hz. Even stronger than in case of model LP2D, the global, asymmetrical expansion of model EP2D on a timescale of several 100 ms is reflected in the fact that significant, or even most, power is in a fundamental, low-frequency signal of a few Hz. Model EP2D emits about $1.3 \times 10^{-13}\ M_{\odot}c^2$ of gravitational wave energy which is about 50% less than model LP2D. In the lower right panels of Figs. 18–21 the thin solid lines correspond to the gravitational wave signal that originates from the incompletely represented (see above) convective region inside the proto-neutron star for model EP2D. A comparison of the thin and thick lines, the latter representing the total signal, shows that most of the emission is produced by the convection in the hot-bubble region. Only at early times after bounce ($t \lesssim 50$ ms, which is when the convective overturn in the neutrino-heated region is not yet fully developed) do convective motions around and inside the neutrinosphere contribute significantly to the total gravitational wave emission (see Fig. 18) at frequencies above 50 Hz (Figs. 19 and 20) and with an integrated energy of about $4.4 \times 10^{-14}\ M_{\odot}c^2$. At later times the signal of convection in the proto-neutron star is minor and the results shown for models ML2D, LP2D, and EP2D in Figs. 18–21 do indeed primarily originate from the mass motions in the hot-bubble region and from the explosive expansion of the supernova.

Comparing the three models we see that with increasing neutrino flux (imposed as an inner boundary condition) and hence with increasing explosion energy the convective activity in the hot-bubble region changes from violent, long-lasting convective overturn associated with accretion processes (model ML2D) to rapid expansion and relatively slowly changing large-scale deformation (model LP2D) which eventually dominate the overall asymmetry and the quadrupole moment of the exploding star (model EP2D). This change of the characteristics of non-radial motions in the hot-bubble and postshock regions is directly reflected in the dominant frequencies of the gravitational wave signal, which drop from about 200 Hz (model ML2D) down to less than 10 Hz (model EP2D). Thus, a measurement of the frequency of the wave signal provides important insights into the explosion dynamics. Moreover, since the signal produced by the convection inside the proto-neutron star is typically of much higher frequency (500–1000 Hz), such a measurement would also allow to discriminate the contributions from both convection zones. Unfortunately, the calculated maximum dimensionless amplitudes $h^{\rm TT}$ (Eq. (11)) are too small to be detected for a supernova outside our own Galaxy, because they lie in the range $|h^{\rm TT}(2D)| \approx 2 \times 10^{-22} \ldots 7 \times 10^{-21}$ for a source at a distance of 10 kpc.

3.3. Three-dimensional results

The analysis of the three-dimensional model caused some problems because our simulation volume involved only a 60 by 60 degree sector of a full sphere. Simply extending the data from the computational volume to the whole sphere by making use of the periodic boundary conditions imposed in angular direction during the simulation did not make sense because a spherical potential was used in the simulation and because the resulting configuration was highly symmetrical in angular direction. The computed sector fits into the full sphere exactly three times in θ-direction and six times in ϕ-direction which gives rise to a 60, 120, and 180 degree rotational symmetry around the z-axis.

In order to compute the gravitational radiation we instead proceeded as follows. First we divided the simulated sector into 36 subsectors of 10 by 10 degree each. Then these 36 subsectors were randomly distributed over the full sphere. This process is justified, because the angular distribution of the dynamical variables varies on scales smaller than or, at least, not much larger than 10 degrees (see Sect. 2.1.2 and Fig. 12). However, one has to take into account that in ϕ-direction the linear extent of the subsectors decreases like $\sin\theta$ when approaching the poles at $\theta = 0$ and $\theta = \pi$. We therefore mapped one 10 by 10 degree subsector as constructed in the simulated 60×60 degree wedge over several pole-near subsectors such that the length scales of the structures were approximately conserved. This mapping procedure of the data was repeated for all radial shells and for all times while keeping the association of $10^{\circ} \times 10^{\circ}$ subsectors of the computational cone with their randomly chosen mapping locations on the sphere fixed.

The resulting angular distribution is displayed in Fig. 22 showing the density on a sphere of radius 65 km (which is right inside the convective layer in the proto-neutron star) at different moments of the evolution. Figure 22 shows that the structures are indeed small enough and the mapping process is random enough to produce statistically homogeneous angular distributions. The result is so perfect that if we omitted the white solid line that marks the boundary of the computed sector, it would be impossible to locate the wedge of the simulation by eye inspection.

Fig. 22. The four panels show the time evolution of the density fluctuations on a sphere with a radius of 65 km located in the middle of the convective layer inside the proto-neutron star. The snapshots are taken at 9.0 ms (top left), 12.2 ms (top right), 13.6 ms (bottom left), and 16.6 ms (bottom right) after the start of the 3D simulation. The ratio of maximum density to minimum density is 1.11, 2.09, 2.32, and 1.72, respectively. In each panel the white frame marks the 60 by 60 degree sector in which the simulation was performed. Note that the fluctuations are homogeneously distributed over the sphere at all times and that the size of the structures increases with time

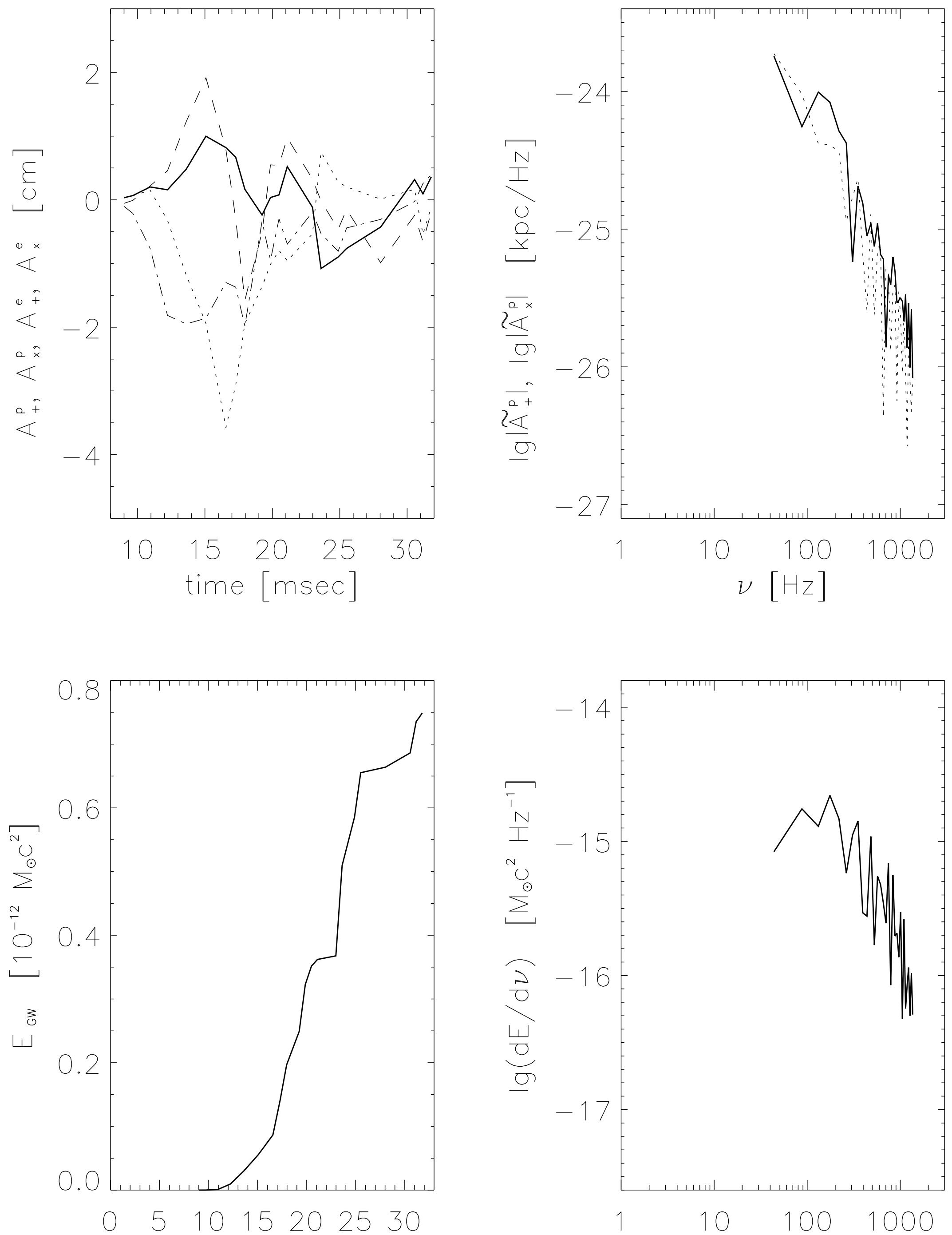

Fig. 23. The gravitational wave signal of convective instabilities inside the proto-neutron star according to the three-dimensional model HB3D. The upper left panel shows the quadrupole waveforms of the two independent signal amplitudes A_+ and $A_\times$ at the pole ($\theta = 0°$, $\phi = 0°$; solid and dotted lines) and at the equator ($\theta = 90°$, $\phi = 0°$; dashed and dashed-dotted lines), respectively. The upper right panel shows the frequency spectra of the polar amplitudes $A^{\rm p}_+$ (solid curve) and $A^{\rm p}_\times$ (dotted curve), the lower left panel the energy radiated in form of gravitational waves, $E_{\rm GW}$ [10^{-12} $M_\odot c^2$], as a function of time, and the lower right panel displays the corresponding spectral energy density

Figure 22 further shows that the angular scale of the fluctuations is time-dependent and grows steadily with time from the onset of the instability at about 9 ms (upper left panel in Fig. 22). The level of the fluctuations reaches a maximum at about 13.6 ms (lower left panel in Fig. 22), when the ratio of maximum to minimum density is 2.32 at 65 km. Within the next 3 ms the ratio drops to a value of 1.72 (lower right panel in Fig. 22) which reflects the increasing homogenization of the mixing layer.

From the density distribution on the full sphere as constructed by the mapping procedure we computed the corresponding three-dimensional gravitational potential taking into account the central point mass (see Sect. 2.1). The three-dimensional Poisson solver employed in the calculation of the potential is an extension of the two-dimensional solver of Müller & Steinmetz (1995) and was provided by Zwerger (personal communication). Using the computed three-dimensional gravitational potential and the mapped density and velocity distributions, we were able to derive the gravitational wave signature of model HB3D from Eqs. (13–23).

According to Fig. 23 model HB3D, which is the three-dimensional analogue of model HB2D, emits significantly less energy in form of gravitational waves. There are several reasons for that. Firstly, the convective elements are smaller, only about half of the typical size found in two dimensions ($l_{3\mathrm{D}} \approx 0.5 l_{2\mathrm{D}}$), and the mass motions are therefore less coherent and do not cause the strong large-scale deformations seen in 2D. Secondly, the rising and sinking convective elements move with smaller velocities in three spatial dimensions, $v_{3\mathrm{D}} \lesssim 5 \times 10^8$ cm/s $\approx 0.5 v_{2\mathrm{D}}$, which leads to reduced over- and undershooting (only about 0.8 instead of 1.2 pressure scale heights, see Sect. 2.1) and is another reason for the weaker large-scale deformation of the outer layers of the proto-neutron star in the 3D model HB3D. While model HB2D emits a gravitational wave energy of $E_{\mathrm{GW}} = 2.2 \times 10^{-9}\ M_\odot c^2$, model HB3D radiates an energy of only $E_{\mathrm{GW}} = 7.5 \times 10^{-13}\ M_\odot c^2$ during the same time interval of 32 ms (compare Figs. 18 and 23). The quadrupole amplitudes of both polarizations (A_+ and $A_\times$) are also shown in Fig. 23 for an observer at the pole and at the equator, respectively. The maximum absolute values of the amplitudes never exceed 4 cm which is about a factor of 200 smaller than in the two-dimensional model HB2D (see Fig. 18). This corresponds to a maximum dimensionless gravitational wave amplitude h^{TT} (Eq. (13)) of $|h^{\mathrm{TT}}(3\mathrm{D})| \approx 2 \times 10^{-22}$ for a source at distance 10 kpc, more than a factor of 30 smaller than in HB2D. A comparison of Figs. 19 and 20 with Fig. 23 (upper and lower right panels, respectively) reveals that the frequency spectrum of the quadrupole amplitude and the spectral energy density show more relative power, respectively are more peaked, towards lower frequencies in case of model HB3D. In HB3D the spectral maxima are around 100–200 Hz and the spectra drop rapidly towards higher frequencies, whereas the amplitude spectrum of HB2D has a broad region of highest power between 100 and 700 Hz (Fig. 18) and the spectral energy density of HB2D peaks between about 200 and 600 Hz. This difference of the wave frequencies is a result of the smaller convective velocities and the correspondingly longer overturn timescales and less violent convection in the three-dimensional situation.

3.4. Gravitational waves from anisotropic neutrino emission

The gravitational wave emission associated with the anisotropic radiation of neutrinos can only be estimated for the presented models because no multi-dimensional neutrino transport was used in the simulations, in fact some of the models were computed without including neutrino effects at all.

In order to estimate the anisotropy parameter $\alpha(t)$ defined in Eq. (29) we used the following procedure. Assuming that the neutrino flux can be approximated by black-body emission and thus scales with the fourth power of the temperature T and with the area $r^2 \mathrm{d}\Omega$ of the emitting surface region, we employed $\mathrm{d}L_\nu(\mathbf{\Omega}, t)/\mathrm{d}\Omega \propto \langle T^4 r^2 \rangle$ to evaluate Eq. (29). Here $\langle T^4 r^2 \rangle$ denotes a mass-weighted radial average of $T^4 r^2$ in the neutrinospheric layer that is considered to encompass densities of $5 \times 10^{10}\ \mathrm{g/cm^3}$ to $10^{11}\ \mathrm{g/cm^3}$. The mean $\langle T^4 r^2 \rangle$ is evaluated by adding up the mass-weighted contributions of all grid cells along a specified radial beam direction $\mathbf{\Omega}$. Repeating this for all angular directions and for all given time levels of a model yields the needed input $\mathrm{d}L_\nu(\mathbf{\Omega}, t)/\mathrm{d}\Omega$ into Eq. (29).

Evaluating the two-dimensional model HB2D we find that the anisotropic neutrino emission associated with the convective processes inside the proto-neutron star leads to an equatorial anisotropy parameter of $\alpha_{\mathrm{e}}(2\mathrm{D}) \approx 10^{-2} \ldots 10^{-1}$ (Eq. (29) with the angular factor of Eq. (27)) at a time when the convective overturn is fully developed ($t \gtrsim 13$ ms after the start of the simulation). We obtain numerical values that are rather close to those of the relative quadrupole moment of $r^2 T^4$. A test integration, moreover, was in agreement with the analytical result for the axially symmetrical case, namely that the corresponding polar anisotropy parameter α_{p} (Eq. (29) with the angular factor of Eq. (26)) is negligibly small. Using the temperature distribution from the three-dimensional simulation HB3D we get $\alpha_{\mathrm{e}}(3\mathrm{D}) \approx \alpha_{\mathrm{p}}(3\mathrm{D}) \approx 5 \times 10^{-4} \ldots 5 \times 10^{-3}$ for $t \gtrsim 13$ ms, again fairly similar to what is obtained from the quadrupole formula.

The anisotropy parameters α therefore turn out to be roughly a factor of 10 smaller in the 3D case than in the 2D situation. Correspondingly, when going from 2D to 3D, the gravitational radiation field h^{TT} (Eq. (28)) becomes about one order of magnitude smaller and the gravitational wave energy E_{GW} (Eq. (31)) approximately two orders of magnitude, if the neutrino luminosities of both cases are similar. Assuming constant luminosity L_ν and anisotropy α for an emission time Δt, one gets

$$R h_\nu^{\mathrm{TT}} \sim 1.6 \times 10^4\ \alpha \left(\frac{L_\nu}{10^{53}\,\mathrm{erg/s}} \right) \left(\frac{\Delta t}{1\,\mathrm{s}} \right)\ \mathrm{cm} \tag{32}$$

and

$$E_{\mathrm{GW},\nu} \sim 1.5 \times 10^{-8}\, \beta\, \alpha^2 \left(\frac{L_\nu}{10^{53}\,\mathrm{erg/s}} \right)^2 \left(\frac{\Delta t}{1\,\mathrm{s}} \right)\ M_\odot c^2\, . \tag{33}$$

For $L_\nu = 10^{53}$ erg/s and a typical emission time of one second – which assumes that convective overturn and anisotropic neutrino emission continue during most of the time when the gravitational binding energy of the proto-neutron star (a few 10^{53} erg) is lost by neutrino emission – one finds $|Rh_\nu^{\mathrm{TT}}(2\mathrm{D})|$ to be of the order of several 100 cm, i.e., $|h_\nu^{\mathrm{TT}}(2\mathrm{D})| \lesssim \mathrm{few} \times 10^{-20}$ for a source at a distance of 10 kpc. The gravitational wave energy is $E_{\mathrm{GW},\nu}(2\mathrm{D}) \lesssim$ few $\times$ $10^{-11}\,M_\odot c^2$. For the three-dimensional case these numbers are $|h_\nu^{\mathrm{TT}}(3\mathrm{D})| \lesssim$ few $\times$ 10^{-21} and $E_{\mathrm{GW},\nu}(3\mathrm{D}) \lesssim$ few $\times$ $10^{-13}\,M_\odot c^2$.

The gravitational wave signal from anisotropic mass motions due to convection inside the proto-neutron star was found (Sects. 3.2 and 3.3) to be $|h^{\mathrm{TT}}(2\mathrm{D})| \lesssim 7 \times 10^{-21}$ and $E_{\mathrm{GW}}(2\mathrm{D}) \approx 2.2 \times 10^{-9}\,M_\odot c^2$ for model HB2D and $|h^{\mathrm{TT}}(3\mathrm{D})| \lesssim 2 \times 10^{-22}$ and $E_{\mathrm{GW}}(3\mathrm{D}) \approx 7.5 \times 10^{-13}\,M_\odot c^2$ for the three-dimensional model HB3D. A comparison shows that the gravitational wave amplitude associated with the neutrino emission is somewhat larger than the wave amplitude due to convective motions. In two dimensions the neutrino gravitational wave amplitude is about 2–3 times larger, in three dimensions the factor can become even 10. The total energy radiated in gravitational waves, however, is dominated by the contributions from the mass quadrupole moment. Neutrino gravitational waves account only for a minor fraction (for a few per cent at most) of the total gravitational wave energy in two-dimensional models, while in 3D they contribute up to several 10% of the gravitational wave energy.

Like the gravitational waves from convective motions inside the newly formed neutron star, the neutrino gravitational waves are predominantly emitted in the frequency band between several 10 Hz and a few 100 Hz because of the common origin and thus similar timescales of the anisotropic processes. In case of the neutrino gravitational waves there is also a superimposed low-frequency component ($\sim$ 1 Hz to a few Hz) caused by the long-time variation of the neutrino emission from the cooling neutron star on a timescale of about one second.

4. Summary and discussion

We have presented two- and three-dimensional simulations of convective instabilities during the first second of a Type II supernova explosion. Convective processes occur in two distinct, spatially well separated regions: (i) inside the proto-neutron star immediately below the neutrinosphere, and (ii) in the neutrino-heated hot-bubble region interior to the outward propagating revived shock front. The convective overturn around and below the neutrinosphere (region (i)) leads to anisotropic neutrino emission which is also a source of gravitational waves. We have calculated the gravitational wave signals from mass motions in both convectively unstable regions and from the aspherical neutrino emission, including the quadrupole waveforms, the power spectra, and the total amount of the emitted gravitational wave energy.

For a supernova located at a distance of 10 kpc the maximum dimensionless gravitational wave amplitudes $|h^{\mathrm{TT}}|$ associated with convective mass motions range from about 2×10^{-22} to 7×10^{-21} and the total amount of the emitted energy varies from 10^{-13} $M_\odot c^2$ to 2×10^{-9} $M_\odot c^2$. Convective motions inside the proto-neutron star involve more mass and are more violent and therefore produce the stronger gravitational wave signal with up to a factor of 10 larger wave amplitudes. However, most of the gravitational radiation from convection inside the proto-neutron star is emitted in the frequency band 100–1000 Hz, while convective motions in the hot-bubble region generate waves from several 100 Hz down to a few Hz.

Comparing different two-dimensional models we find that with increasing total neutrino luminosity and hence with increasing explosion energy the convective activity in the hot-bubble region changes from violent convective overturn associated with anisotropic accretion processes to rapid overall expansion and relatively slowly changing large-scale deformations of the expanding shells behind the outward propagating supernova shock. This change of the characteristics of non-radial motions in the hot-bubble region is directly reflected in the dominant frequencies of the gravitational wave signal. While turbulent overturn around the proto-neutron star produces gravitational waves with most power at frequencies of 100–200 Hz, the dominant frequencies are at only some 10 Hz when the period of convective activity is short and the non-sphericity of the model is determined by the explosive expansion. Thus, a measurement of the frequency of the wave signal would provide important insights into the explosion dynamics. Moreover, since the signal produced by the convection inside the proto-neutron star is typically of much higher frequency (about 1000 Hz), it would also be possible to discriminate the contributions from the two convection zones to the measured signal. Interestingly, structures in the gravitational wave signal are well correlated with prominent features in the neutrino emission if both gravitational wave and neutrino production are associated with dynamical processes in and around the nascent neutron star. Simultaneous information from both neutrino and gravitational wave measurements would therefore impose important contraints on theoretical models of Type II supernova explosions.

The anisotropic neutrino emission itself generates gravitational waves, too. We estimate the degree of anisotropy from the density and temperature inhomogeneities associated with convective and turbulent processes in the neutrinospheric region. We find that for typical post-bounce neutrino luminosities the gravitational wave amplitude can be larger than the wave amplitude due to mass motions by a considerable factor of 2–10, although the energy in the neutrino tidal field is only a minor contribution to the total energy radiated in gravitational waves.

Our three-dimensional simulation of convection inside the proto-neutron star gives a strongly reduced gravitational wave signal compared to the corresponding two-dimensional model. The main reason for this is that in three spatial dimensions the convective structures and elements are smaller ($l_{\mathrm{3D}} \approx 0.5 l_{\mathrm{2D}}$), move less fast ($v_{\mathrm{3D}} \lesssim 5 \times 10^8$ cm/s $\approx 0.5 v_{\mathrm{2D}}$), and, correspondingly, show less strong overshooting and undershooting (0.8 instead of 1.2 pressure scale heights). The maximum quadrupole amplitudes due to mass motions are reduced by more than a factor of 30, the gravitational wave amplitudes associated with the anisotropic neutrino emission by as much as a factor of 10. The total amount of energy radiated in form of gravitational waves is 2–3 orders of magnitude smaller in 3D. A similarly strong reduction of the signal strength is to be expected for the gravitational waves emitted by turbulent motions in the hot-bubble region when the simulations will be performed in three spatial dimensions.

The gravitational wave signal from convective and turbulent processes inside the nascent neutron star and in the surrounding neutrino-heated region is rather weak compared with other potential astrophysical sources of gravitational waves. Neutron star mergers produce signals that are about 100–1000 times stronger with dimensionless wave amplitudes $|h^{\mathrm{TT}}|$ of up to (3–4) $\times 10^{-18}$ for a source at 10 kpc distance (for recent calculations, see, e.g., Ruffert et al. 1996 and references therein). Two-dimensional simulations of the gravitational collapse of rotating stellar cores with realistic input physics yield maximum wave amplitudes of 2×10^{-20} (Mönchmeyer et al. 1991). Computing a broad variety of models with different angular momentum and different angular momentum distribution in the pre-collapse stellar core and considering different equations of state during core collapse, Zwerger (1995) and Müller & Zwerger (1995) found that the most efficient models have $|h^{\mathrm{TT}}| \lesssim 10^{-19}$. However, their most weakly emitting two-dimensional models produced wave amplitudes about one order of magnitude smaller than the maximum signal that can be expected from the simulations presented in this paper.

Our results are in rough qualitative agreement with the findings of Burrows & Hayes (1996) based on two-dimensional models, although there are quantitative differences. We emphasize that the results for the gravitational wave signal associated with non-spherical neutrino emission depend sensitively on the duration of the phase of anisotropic neutrino loss and on the temporal evolution of the total luminosity in all kinds of neutrinos. These characteristics will vary with the properties of the exploding star and thus with the parameters of the forming neutron star and will also be sensitive to the details of the numerical scheme and physical input used for the simulations. Moreover, calculations based on two-dimensional models tend to overestimate the gravitational wave emission by about one order of magnitude.

The models that were analysed in this work are only another preliminary step towards the full, complex problem of stellar core collapse and supernova explosion in three dimensions and towards a detailed quantitative understanding of the associated emission of gravitational waves. We have performed hydrodynamical calculations in two and three dimensions and have analyzed the effects of post-bounce convective activity in the forming neutron star and in the exploding star. However, our models have a number of restrictions and approximations. These will have to be removed and their possible and probable quantitative influence on the presented results will have to be investigated in future work.

Our simulations did start from progenitor star models that were neither evolved to the onset of core collapse in two or three dimensions, nor followed through core collapse and bounce with a multi-dimensional code, although the multi-dimensional description of these evolutionary phases could be important to determine the structure of the initial state of our computations, even in the case that rotation is absent in the star (see, e.g., Bazan & Arnett 1994; Burrows et al. 1995; Goldreich et al. 1995). Furthermore, self-consistency was violated by mapping the initial configuration of a collapsed stellar core as given from a one-dimensional, general relativistic simulation into our multi-dimensional code which treated gravity in the Newtonian approximation. In addition, only in the two-dimensional runs non-sphericities of the gravitational potential were taken into account via an expansion into spherical harmonics, whereas in the 3D simulations a spherically symmetrical potential derived from the mean density distribution was used. Moreover, the neutrino physics in the current models needs to be improved or even waits for being included in the multi-dimensional modelling. Finally, current progenitor star models and the presented supernova simulations assume zero angular momentum. With the combined effects of rotation, convection inside the proto-neutron star, and neutrino-driven overturn in the hot-bubble region, however, the quantitative results of the gravitational wave emission could be significantly modified.

Acknowledgements. The post-collapse models provided to us by S.W. Bruenn and W. Hillebrandt to be used as initial models in our simulations are kindly acknowledged. We would like to thank Maximilian Ruffert, Gerhard Schäfer, and Thomas Zwerger for many enlightening discussions and valuable comments. In particular, we are grateful to Thomas Zwerger for providing to us his 3D Poisson solver. All hydrodynamical simulations were performed on the CRAY-YMP 4/64 of the Rechenzentrum Garching. The Rechenzentrum Garching is also acknowledged for generous financial support concerning the publication costs.

References

Bandiera R., 1984, A&A 139, 368
Bazan G., Arnett D., 1994, ApJ 433, L41
Bethe H.A., Wilson J.R., 1985, ApJ 295, 14
Bethe H.A., 1990, Rev. Mod. Phys. 62, 801
Blanchet L., Damour T., Schäfer G., 1990, MNRAS 242, 289
Bonazzola S., Marck J.A., 1993, A&A 267, 623
Bruenn S.W., 1993, in: Nuclear Physics in the Universe, eds. M.W. Guidry and M.R. Strayer, IOP, Bristol, p. 31
Burrows A., 1987, ApJ 318, L57
Burrows A., Fryxell B.A., 1992, Sci 258, 430
Burrows A., Fryxell B.A., 1993, ApJ 418, L33
Burrows A., Hayes J., 1996, Phys. Rev. Lett. 76, 352
Burrows A., Hayes J., Fryxell B.A., 1995, ApJ 450, 830
Burrows A., Lattimer J.M., 1988, Phys. Rep. 163, 51
Colella P., Woodward P.R., 1984, J. Comp. Phys. 54, 174
Colgate S.A., 1989, Nature 341, 489
Colgate S.A., Herant M., Benz W., 1993, Phys. Rep. 227, 157
Epstein R., 1978, ApJ 223, 1037
Epstein R.I., 1979, MNRAS 188, 305
Fryxell B.A., Müller E., Arnett W.D., 1989, MPA-Preprint 449, Max-Planck-Institut für Astrophysik, Garching
Fryxell B.A., Müller E., Arnett W.D., 1991, ApJ 367, 619

Goldreich P., Lai D., Sahrling M., 1995, in: Unresolved Problems in Astrophysics, eds. J.N. Bahcall and J.P. Ostriker, Cambridge University Press, Cambridge, in press
Hachisu I., Matsuda T., Nomoto K., Shigeyama T., 1990, ApJ 358, L57
Hachisu I., Matsuda T., Nomoto K., Shigeyama T., 1991, ApJ 368, L27
Herant M., Benz W., 1991, ApJ 345, L412
Herant M., Benz W., 1992, ApJ 387, 294
Herant M., Benz W., Colgate S.A., 1992, ApJ 395, 642
Herant M., Benz W., Hix W.R., Fryer C.L., Colgate S.A., 1994, ApJ 435, 339
Hillebrandt W., 1987, in: High Energy Phenomena Around Collapsed Stars, ed. F. Pacini, Reidel, Dodrecht, p. 73
van den Horn L.J., van Weert C.G., 1981, ApJ 251, L97
Janka H.-Th., 1993, in: Frontier Objects in Astrophysics and Particle Physics, eds. F. Giovannelli and G. Mannocchi, Società Italiana di Fisica, Bologna, p. 345
Janka H.-Th., Müller E., 1993a, in: Frontiers of Neutrino Astrophysics, eds. Y. Suzuki and K. Nakamura, Universal Academy Press, Tokyo, p. 203
Janka H.-Th., Müller E., 1993b, in: Supernovae and Supernova Remnants, eds. R. McCray and Zhenru Wang, Cambridge Univ. Press, Cambridge, p. 109
Janka H.-Th., Müller E., 1995a, Phys. Rep. 256, 135
Janka H.-Th., Müller E., 1995b, ApJ 448, L109
Janka H.-Th., Müller E., 1996, A&A, to appear in Feb. 1 issue
Miller D.S., Wilson J.R., Mayle R.W., 1993, ApJ 415, 278
Misner C.W., Thorne K.S., Wheeler J.A., 1973, Gravitation, chap. 35, Freeman, San Francisco, USA
Mönchmeyer R, Schäfer G., Müller E., Kates R.E., 1991, A&A 246, 417
Müller E., 1993, in: Proc. of the 7th Workshop on Nuclear Astrophysics (Ringberg Castle, March 22-27, 1993), eds. W. Hillebrandt and E. Müller, Report MPA/P7, Max-Planck-Institut für Astrophysik, Garching, p. 27
Müller E., Janka H.-Th., 1994, in: Reviews in Modern Astronomy 7, Proceedings of the International Scientific Conference of the AG (Bochum, Germany, 1993), ed. G. Klare, Astronomische Gesellschaft, Hamburg, p. 103
Müller E., Steinmetz M., 1995, Comp. Phys. Commun. 89, 45
Müller E., Zwerger T., 1995, Ann. N.Y. Acad. Sci. 759, 498
Müller E., Fryxell B.A., Arnett W.D., 1991, in: ESO/EIPC Workshop on SN 1987A and other Supernovae, ESO Workshop and Conference Proceedings No. 37, eds. I.J. Danziger and K. Kjär, ESO, Garching, p. 99
Nakamura T., Oohara K., 1989, in: Frontiers in Numerical Relativity, eds. C.R. Evans, L.S. Finn, and D.W. Hobill, Cambridge Univ. Press, p. 254
Ruffert M., Janka H.-Th., Schäfer G., 1996, A&A, in press; MPA-Preprint 889
Shimizu T., Yamada S., Sato K., 1993, PASJ 45, L53
Shimizu T., Yamada S., Sato K., 1994, ApJ 432, L119
Thorne K.S., 1980, Rev. Mod. Phys. 52, 299
Thorne K.S., 1995, Proc. of the Snowmass 95 Summer Study on Particle and Nuclear Astrophysics and Cosmology, eds. E.W. Kolb and R. Peccei, World Scientific, Singapore, in press
Turner M.S., 1978, Nat 274, 565
Wilson J.R., 1985, in: Numerical Astrophysics, eds. J.M. Centrella, J.M. LeBlanc, and R.L. Bowers, Jones and Bartlett, Boston, p. 422
Wilson J.R., Mayle R., Woosley S.E., Weaver T., 1985, Ann. N.Y. Acad. Sci. 470, 267
Yamada S., Shimizu T., Sato K., 1993, Prog. Theor. Phys. 89, 1175
Zwerger T., 1995, PhD Thesis, Technische Universität München

This article was processed by the author using Springer-Verlag LaTeX A&A style file *L-AA* version 3.